T.R.
BOLU ABANT İZZET BAYSAL UNIVERSITY
INSTITUTE OF GRADUATE STUDIES

A STUDY ON INVESTIGATION OF FCNC tqZ COUPLINGS VIA νZp PRPUDUTION AT FUTURE ELECTRON-PROTON COLLIDERS

MASTER OF SCIENCE

HANEEN YOUSIF

BOLU, DECEMBER - 2022

T.R.
BOLU ABANT İZZET BAYSAL UNIVERSITY
INSTITUTE OF GRADUATE STUDIES
Department of Physics

A STUDY ON INVESTIGATION OF FCNC tqZ COUPLINGS VIA νZp PRPUDUTION AT FUTURE ELECTRON-PROTON COLLIDERS

MASTER OF SCIENCE

HANEEN YOUSIF

ACADEMIC SUPERVISOR
Prof. Dr. Haluk DENIZLI

BOLU, DECEMBER - 2022

APPROVAL OF THE THESIS

A Study on Investigation of FCNC tqZ Couplings via νZp production at Future Electron - Proton Colliders submitted by **HANEEN YOUSIF** and defended before the Examining Committee Members listed below in partial fulfillment of the requirements for the degree of **Master of Science** in **Department of Physics, Institute of Graduate Studies of Bolu Abant Izzet Baysal University in 12.12.2022** by

Examining Committee Members	**Signature**
Supervisor Prof. Dr. Haluk DENİZLİ Bolu Abant Izzet Baysal University	....
Member Prof. Dr. Abdulkadir ŞENOL Bolu Abant Izzet Baysal University	....
Member Prof. Dr. İlkay TÜRK ÇAKIR Ankara University	....

Prof. Dr. İbrahim KÜRTÜL

Director of Instıtute of Graduate Studies

ETHICAL DECLARATION

In this thesis dissertation that was properly prepared according to the Thesis Writing Rules of Bolu Abant İzzet Baysal University of the Institute of Graduates Studies, I hereby declare that;

- All data, information, and documents presented in the thesis were obtained in accordance with the academic and ethical rules,
- All data, documents, assessments, and results were presented in accordance with the scientific ethical and moral rules,
- All works that were benefitted in the thesis were appropriately cited,
- No alteration was made in the data used,
- Study presented in this thesis is original,

Otherwise, I declare that I accept the loss of all my rights in case any contradiction that may arise against me.

Based on the plagiarism report that was generated on the date of 17/12/2022 by using predetermined filtrations set by Directorate of Institute of Graduate Studies of the Turnitin programme, a plagiarism detection software, the similarity index detected was 26 %.

____

HANEEN YOUSIF

ABSTRACT

A STUDY ON INVESTIGATION OF FCNC tqZ COUPLINGS VIA ν Z P PRODUCTION AT FUTURE ELECTRON-PROTON COLLIDERS

MSC THESIS
HANEEN YOUSIF

BOLU ABANT IZZET BAYSAL UNIVERSITY
INSTITUTE OF GRADUATE STUDIES
DEPARTMENT OF PYSICS
(SUPERVISOR: HALUK DENIZLI)

BOLU, DECEMBER 2022
(xv +60)

In the standard model, top quark flavor changing neutral currents are absent at the tree-level. As a consequence, processes involving these currents can be generated at loop-level and thus are expected to be strongly suppressed. Nevertheless, they can be enhanced in the presence of new physics beyond the standard model and tested at future colliders with high energy. In this thesis, we investigate the top quark anomalous flavor changing neutral current tqZ within the framework of effective field theory to probe the best limits on the tqZ couplings, namely K_{ut}andK_{ct}, via single top production in the e p → υ_e Z q process at the future LHeC and FCC-he colliders. The signal and SM background events are generated using a Madgraph and Delphes was used to include realistic detector effects. We have found that the cross sections of the signal increase remarkably when we take large values of the couplings and set K_{ut}=K_{ct}. In addition, we have studied the kinematic distributions of the final states particles and found that applying certain cuts can enhance the signal. Our study shows that the FCC-he gives the best limits for the BR (t → qZ) for (Z→ $\ell\ell$) = 4×10^{-4}.

KEYWORDS: Top quark, Flavour Changing Neutral Current, Beyond the standard model, Future electron-proton colliders.

ÖZET

FCNC tqZ KUPLAJLARININ ν Z P ÜRETİMİ YOLUYLA GELECEK ELEKTRON-PROTON ÇARPIŞTIRICILARINDA İNCELENMESİ ÜZERİNE BİR ÇALIŞMA

YÜKSEK LİSANS TEZİ
HANEEN YOUSIF
BOLU ABANT İZZET BAYSAL ÜNİVERSİTESİ
LİSANSÜSTÜ EĞİTİM ENSTİTÜSÜ
FIZIK ANABİLİM DALI

(TEZ DANIŞMANI: HALUK DENIZLI)

BOLU, ARALIK - 2022
(xv + 60)

Standart modelde, ağaç seviyesinde üst kuark çeşnisini değiştiren nötr akımlar yoktur. Sonuç olarak, bu akımları içeren süreçler döngü düzeyinde üretilebilir ve bundan dolayı güçlü bir şekilde bastırılmaları beklenir. Bununla birlikte, standart modelin ötesinde yeni fiziğin varlığında geliştirilebilir ve gelecekteki yüksek enerjili çarpıştırıcılarda test edilebilirler. Bu tezde, tqZ kuplajları, K_{ut} ve K_{ct}, üzerindeki en iyi limitleri e p → υ_e Z q süreci ile gelecekteki LHeC ve FCC-he çarpıştırıcılarında üst kuark anormal çeşni değiştiren nötr akımını efektif alan teorisi çerçevesinde inceledik. Sinyal ve SM arka plan olayları Madgraph kullanılarak oluşturulmuştur ve gerçekçi dedektör efektlerini dahil etmek için ise Delphes kullanılmıştır. Kuplajların büyük değerlerini aldığımızda ve $K_{ut} = K_{ct}$ olarak ayarladığımızda, sinyal tesir kesitlerinin belirgin şekilde arttığını bulduk. Ayrıca, son durum parçacıklarının kinematik dağılımlarını inceledik ve belirli kestirmelerin uygulanmasının sinyali iyileştirebileceğini gördük. Çalışmamız FCC-he'nin en iyi limitleri için BR (t → qZ) for (Z→ $\ell\ell$) $= 4 \times 10^{-4}$ verdiğini göstermektedir.

ANAHTAR KELİMELER: Üst Kuark, Çeşni Değiştiren Nötr Akım, Standart Model Ötesi, Gelecek Elektron-Proton Çarpıştırıcıları.

TABLE OF CONTENTS

LIST OF FIGURES

Page

LIST OF TABLES

Page

LIST OF ABBREVIATIONS AND SYMBOLS

SM **:** Standard Model

BSM **:** Beyond Standard Model

FCNC **:** Flavor Chanching Neutral Current

LHeC **:** Large Hadron Electron Collider

FCC-he **:** Future Circular Collider hadron electron

ATLAS : A Toroidal LHC Apparatus.

CERN : Conseil Europeen pour la recherche nucleaire

CMS : Compact Muon Solenoid

HE-LHC : High Energy Large Hadron Collider

UMN : University of Minnesota

NP : New Physics.

GeV : Giga -Electron Volt

BDT : Boosted Decision Tree

LHC : Large Hadron Collider

C.L. : Confidence level

TeV **:** Tera-Electron Volts

L_{int} : Integrated luminosity

P^T : Transverse momentum

η : Pseudo-rapidity

MET : Missing Transverse Energy

ACKNOWLEDGEMENTS

First and foremost, I am grateful to Almighty Allah for providing me with love, strength, capability, as well as for the opportunity to accomplish my thesis patiently. Day by day, I have felt your guidance, and I will keep putting my faith in you for whole my life.

Also, I would like to express special thanks and gratitude to my respected supervisor Prof. Dr. Haluk Denizli for his great effort, guidance, kindness, and professional advice in finishing this study. Thank you for your brilliant remarks and suggestions and I truly appreciate every minute that you have spent teaching and mentoring me.

Also, I would like to thank Prof. Dr. Abdulkadir Şenol for his kindness, and his contribution to the preparation of this study. Thank you for being so cooperative with all of us, which allowed me to inquire about many questions.

I would like to thank the committee members, the institute of graduate studies, and the members of the physics department at Bolu Abant Izzet Baysal University, where I accomplished my post graduate studies.

I would not forget my friends who helped and motivated me to continue this work, I am blessed to have you all, thank you from the bottom of my heart.

Last but not least, I would like to express my sincere gratitude to all my family members, particularly my parents, for their unconditional support, and persistent encouragement, without you this study would not have been possible.

1. INTRODUCTION

Particle physics is a branch of modern physics that is concerned with particles at the subatomic scale and the main forces acting on them. It aims to increase our comprehension of the construction of the Universe at this microscopic scale. This in turn can help us to find answers to some important questions regarding the predominance of matter over anti-matter in our Universe in what is recognized as the Universe's baryon asymmetry. In addition, creating particles and anti-particles in accelerators with high energy in conditions resembling the moments after the big bang allows us to understand the conditions of the early Universe at that moments. As a consequence, we can learn about the evolution of the Universe which is in a state of continuous evolution to other phases. Among other goals of particle physics is to inspect questions like how many kinds of fundamental forces and particles exist in our Universe, and how they interact with each other (1).

The Standard Model (SM) has provided the most accurate explanation of the universe at the sub-atomic scale. Since the early formulation of the SM, it has shown to be extremely effective in describing the available experimental observation. In an attempt to improve the theoretical comprehension of the SM, a new stimulus for physics beyond the SM emerged. This stimulus has sparked a variety of experiments. It has had to postulate new physics beyond the SM since some couplings and masses in the SM, as defined by experiments, seem to need better clarification (2). In the SM, the top quark is known to be the heaviest fundamental particle Thus, it decays rapidly to other SM particles before hadronization. Therefore, it has been utilized in the literature as a possible window to investigate novel physics processes.

The thesis is structured as follows, in chapter 1, we give a concise to the Standard Model as well as summarize the properties, production, and decays of the top quark, in addition to the theoretical framework which includes the effective Lagrangian required for the calculation of the top quark FCNC decay width ($t \rightarrow qZ$) and the branching ratios of the decay modes needed in the study. Chapter 2, concentrates on the novel features and the capabilities of the two future hadron electron colliders (LHeC) and (FCC-he) concerning the physic program to be explored. The aim and scope of this thesis will be introduced in chapter 3. Finally, in chapter 4, we present our analysis and result for the cross-section of the e p→ υ_e Z p process, and the kinematic distributions of the final state particles at each collider. Moreover, based on our computations of the statistical significance, we will provide our results of the upper limits of the BR (t → qZ) and present a comparison with the related previous studies.

1.1 Standard Model

The standard model (SM) precisely expresses the characteristics and interactions of the subatomic particles. Currently, it is the best model that depicts the main structure of matter and the interaction of elementary particles. This can be understood as SM predictions were confirmed, for instance, the discovery of the top-quark and the Higgs boson. The SM is based on a relativistic quantum field theory which ensures the local SU (3) x SU (2) x U (1) gauge symmetry. A. Salam, S. Glashow and S. Weinberg formulated the SM in the mid-1970s (3–5).

In the SM, there are two kinds of subatomic particles which known as fermions and bosons. Fermions are matter particles with a half-integer spin while boson have integer spin such as photons, gluons, Z and W ± bosons. Fermions are classified into leptons and quarks.

Quarks are massive particles and have electrical and color charge. There are 6 flavors of quarks that are arranged according to their spin to up-type quarks with electric charge Q = +2/3 and down-type quarks with electric charge Q = -1/3. Up-type quarks include up (u) quark, charm (c) quark, and top or truth (t) quark. Down-type quarks include down (d), strange (s), beauty, or bottom (b), they are listed in tale 1.1. In addition, for each quark, there is an anti-quark of the same mass but with an electric charge of the opposite sign. Quarks come in three-generation, the first generation of quarks has the lightest masses and thus quarks in this generation are stable. Quarks can interact through gravitational, electromagnetic, and weak forces. Moreover, they can interact also through strong nuclear forces as they have color charges (1).

Leptons include two types of particles: the neutrinos which are neutral particles and the electrically charged particles namely, the electron, the muon, and the tau particles (e, μ, τ). Leptons are classified into three generations as listed in Table 1.1. Additionally, for each lepton, there is an anti-lepton, which has the same mass but with an opposite electric charge. In the SM the neutrinos are massless. However, neutrino oscillation, which was observed experimentally, indicates that they have a very small mass (6).

Table 1.1. An overview of the masses and electric charges of the three families of Standard Model leptons and quarks (7).

Quarks				Leptons			
Particle		Q (q_e)	Mass GeV	Particle		Q (q_e)	Mass GeV
Up	u	+2/3	0.002	Electron	e	-1	0.000511
Down	d	-1/3	0.005	e neutrino	ν_e	0	$< 10^{-9}$
Strange	s	-1/3	0.1	Muon	μ	-1	0.106
Charm	c	+2/3	1.2	μ neutrino	ν_μ	0	$< 10^{-9}$
Bottom	b	-1/3	4.2	Tau	τ	-1	1.78
Top	t	+2/3	173	τ neutrino	ν_τ	0	$< 10^{-9}$

In the standard model, there are three kinds of essential forces (interactions); the strong nuclear force, the weak nuclear force, and the electromagnetic force. On the other hand, the gravitational force is not included in the SM. In view of quantum field theory, these forces are mediated by the exchange of gauge bosons. Specifically, the W and Z bosons are the mediators of the weak interaction while the mediator of the electromagnetic force is the photon. Finally, the strong force was explained by Fritsch and Gell-Mann in 1973 (8). It is mediated by 8 massless gluons. The forces associated with the corresponding bosons and their properties are listed in Table 1.2.

Table 1.2. Summary of the gauge bosons of the SM, given with their properties and associated interactions (9).

Bosons	Interaction	Electric charge	Mass
γ	Electromagnetic	0	$< 1 \times 10^{-18}$GeV
$W^{\pm}$	Weak	± 1	$80.385^{\pm}$ 0.015 GeV
Z	Weak	0	$91.1876^{\pm}0.0021$GeV
g	Strong	0	0

Bosons have integer spins that can be 0, 1, 2, and so on. Bosons with spin 0 are called scalars such as Higgs boson while bosons with spin 1 are called vector bosons such as the gauge bosons mediating the forces listed in Table 1.2 above.

Since the weak bosons are relevant to our study, we focus below on these bosons.The Z boson has a mass m_Z = 91.1875 ± 0.0021 GeV, full width Γ_Z = 2.4952 ± 0.0023 GeV and it is electrically neutral. W± has mass of approximately 80 GeV and a full width Γ_W of around 2 GeV (10). The mechanism responsible for generating the masses of the W and Z bosons is known as the Higgs mechanism. One of the consequences of this mechanism is the presence of the Higgs boson which is a scalar boson that was observed as the last component of the Standard Model (SM) in 2012 (11). It was discovered at the Large Hadron Collider (LHC) at 2012 with a mass equal to 125.5 GeV (11). The Higgs boson has rare features. For instance, it is a scalar field, contrary to every other field of the standard model. Its important role is to trigger a crucial mechanism that gives masses to the massive particle in the SM. For instance, the masses of the charged fermions are obtained through Yukawa interactions between the fermions and the Higgs field (12-13).

1.2 Properties of top quark

At Fermilab, the top quark was discovered, in 1995(14–15). In the SM, the top quark has an electric charge of +2/3. Exotic models, nevertheless, have been put out in which the top quark can still decay to a W boson and a b quark despite having a charge of -4/3. The top quark charge must still be determined experimentally in order to emphasize that the discovered top quark is the SM top quark. The likelihood that top quarks have a charge of -4/3 has been evaluated by the CDF (16), D0 (17), and ATLAS (18) experiments, and it has been determined that the SM value is preferred. The present measurement (18), which eliminates charge -4/3 at more than 8 standard deviations, has determined that the charge of the top quark is equal to 0.64 ± 0.02 (stat) ± 0.08 (syst).

The top quark, which according to the SM is the heaviest subatomic particle.Its mass (m_t) is a crucial parameter of the SM and is not foreseen by the model. The value of m_t has been determined in a diversity of final states and using an assortment of techniques. In several of these attempt to reconstruct the top quark from its decay products and fit the invariant mass of that combination of particles, while others deduce the value of m_t based on the cross-section on of top quark pair or single top quark production. A summary of the most recent computations is presented in figure 1.1, obtaining the final accurate rates from CMS mass of the top quark = 172.44 ± 0.48 GeV (19) compared to ATLAS's m_t = 172.69 ± 0.48 GeV (20). The outcomes are contrasted with those obtained using the LHC and the Tevatron + LHC.

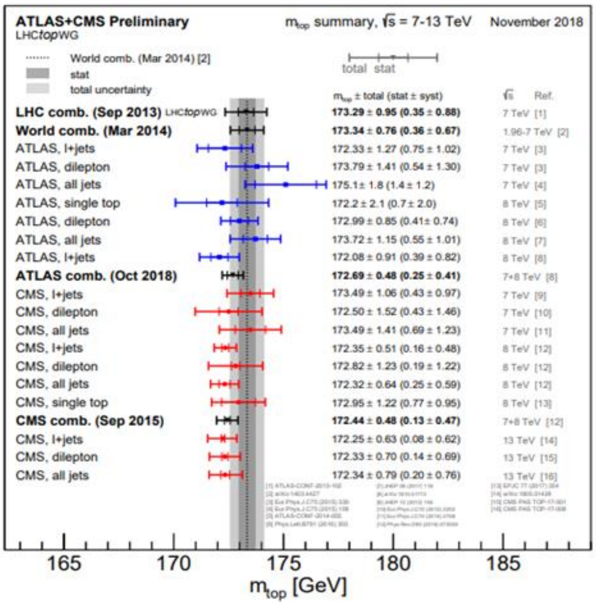

Figure 1.1. Synopsis of the top quark decay measurements from CMS and ATLAS (21).

Due to being m_t significantly above the W b threshold, the decay t →W $_b$ is predictable to dominate the top quark width. Neglecting small terms of order $\frac{m_b^2}{m_t^2}$, where m_b depicts the mass of the b quark, and higher-order weak corrections, the top quark width in the SM at NLO is anticipated (22) to be

$$\Gamma_t^{(0)} = \frac{G_F m_t^3}{8\pi\sqrt{2}}(1 - r^2)^2(1 + 2r^2) \qquad (1.1)$$

Where $$r^2 = \frac{m_W^2}{m_t^2} \quad (1.2)$$

$$\Gamma_t = \frac{G_F m_t^3}{8\pi\sqrt{2}} |V_{tb}|^2 \left(1 - \frac{M_W^2}{m_t^2}\right)^2 \left(1 + 2\frac{M_W^2}{m_t^2}\right)\left[1 - \frac{2\alpha_s}{3\pi}\left(\frac{2\pi^2}{3} - \frac{5}{2}\right)\right] \quad (1.3)$$

where M_W represents the mass of the W boson and $|V_{tb}|$ set to 1, G_F is the Fermi constant, α_s stands for the strong coupling constant $\Gamma_t = 1.35\ GeV/c^2$ when $m_t = 173.3\ GeV$ utilizing $\alpha_s = 0.118$ a m_t equal to 172.5 GeV, for m_t= 172.5 GeV, the Γ_t at NLO equal to 1.33 GeV. According to a current next-to-next-to-leading-order (NNLO) computation, Γ_t = 1.32 GeV (23). Moreover, the value of Γ_t can alter in new physics from what the SM foresees.

1.3 Top quark production and decays

There are two ways to produce top quark, either singly by electroweak interaction or as pairs, through the strong interaction. Top quarks are mostly created in pairs in the LHC and Tevatron hadron colliders through strong interactions, gluon fusion, and $q\bar{q}$ annihilation processes. Relying on the collider center-of-mass-energy (√s), and on the kind of particle beams being utilized ($p\bar{p}$ or pp), the two processes are different in their relative importance. At the Tevatron $p\bar{p}$ collider, occurs at the √s of 1.96 TeV, is produced in the quark-antiquark ($t\bar{t}$) annihilation at approximately 85%, while at the LHC, when pp collisions happen at 7 TeV, collider $t\bar{t}$ production arises from gluon-gluon fusion (24) ($gg \rightarrow t\bar{t} \approx 80\%$).

Production of top-pairs can be also by the weak interaction when two quarks interchange γ or Z^0 the cross-section of top quark pair production has been calculated by the LHC at the $\sqrt{s}$ of 13 TeV to be $\sigma_{t\bar{t}} = 831.8^{+19.8+35.1}_{-29.2-35.1}$ pb and $\sigma_{t\bar{t}} = 252.9^{+6.1+11.5}_{-8.6-11.5}$ pb (25) at $\sqrt{s}$ = 8 Tev considering the mass of top-quark of m_t = 172.5 GeV.

Because of the enormous mass of the top quark, the phase space available for top quark decay is huge. The decay of the top quark is categorized according to the decay modes of the W boson. Thus, the top quark can decay into pair of different quarks or into pair of charged and its corresponding (anti) neutrino.

When considering the $t\bar{t}$ production, the top quark decay modes are categorized based on the decays of the two W bosons. The essential decay channels are then included (26).

- Dilepton channel with 10% branching ratio.
- Hadronically with a BR of nearly 46%.
- Final states, which are classified as semileptonic events and frequently refer to as $\ell + jets$.

These channels are obtained when one of the two W bosons decays leptonically while the other W decays hadronically.

1.4 FCNC top quark interaction in beyond the standard model

Flavor Changing Neutral Current (FCNC) is a transition that alters the flavor of a fermion without changing its electric charge. According to the Glashow-Iliopoulos-Maiani (GIM) mechanism (27), FCNC transitions such as $t \rightarrow qZ$, where q is up or c quark, are absent in the SM at the tree level and only can take place at the loop level. Since the anticipated FCNC transitions of the top quark are much larger compared to other quarks, searches for top quark FCNC transitions have motivated a lot of studies in the literature within diverse models beyond the SM. In particular, studies within BSM physics might significantly improve FCNC processes. With the ongoing and planned search of such processes at current and future colliders, any observation of a top quark FCNC interaction can point to the presence of new physics.

On the experimental side, CDF (28), D0 (29), ATLAS (30), and CMS (31) collaborators have searched for $t \rightarrow Zq$ channel in the decays of the produced top pair $t\bar{t}$ events. In the performed search, the decays of the Z bosons to light charged leptons pairs e^+e^- or $\mu^+\mu^-$ are used to identify them. The result of the search set the best limit BR ($t \rightarrow Zq$) greater than 0.05% is eliminated at 95% CL. With data acquired at the $\sqrt{s}$ of 8 TeV and 7 TeV respectively, using 5.0 fb^{-1} and 19.7 fb^{-1}, the CMS search was able to reach this limit.

1.5 Anomalous FCNC top interaction (details of effective Lagrangian)

This section provides a concise explanation of the theoretical framework for top FCNC on which our study is based. The FCNC couplings between the top quark, a light quark, and a Z boson are described utilizing an effective Lagrangian approach in the $tq\gamma$ and tqZ, the FCNC Lagrangian anomalous interaction can be defined as (32):

$$L_{eff} = \frac{g_e}{2m_t}\bar{t}\sigma^{\mu\nu}(\lambda_u^L P_L + \lambda_u^R P_R)uA_{\mu\nu} + \frac{g_e}{2m_t}\bar{t}\sigma^{\mu\nu}(\lambda_c^L P_L + \lambda_c^R P_R)cA_{\mu\nu} \quad (1.4)$$

$$+ \frac{gW}{4c_W m_z}\bar{t}\sigma^{\mu\nu}(k_u^L P_L + k_u^R P_R)uZ_{\mu\nu} + \frac{gW}{4c_W m_Z}\bar{t}\sigma^{\mu\nu}(k_c^L P_L + k_c^R P_R)cZ_{\mu\nu} + h.c.$$

where $g_e(g_W)$ refers to the electromagnetic (weak) coupling constant; c_W is the cosine of the weak mixing angle; $\lambda_q^{L(R)}$ and $k_q^{L(R}$ denote the strengths of anomalous top FCNC tqγ and tqZ couplings, with q indicating an up or charm quark, which disappear at the leading order in the SM and $P_{L(R)}$ stands for the left (right) handed projection operators. The photon field strength tensor is define as $A_{\mu\nu} = \partial_\mu A_\nu - \partial_\nu A_\mu$ and Z boson field strength tensor is given by $Z_{\mu\nu} = \partial_\mu Z_\nu - \partial_\nu Z_\mu$, and the anti-symmetric tensor $\sigma^{\mu\nu} = \frac{i}{2}[\gamma^\mu, \gamma^\nu]$. The effective Lagrangian L_{eff} is used to compute decay rates (for channels tqγ and tqZ) as well as production cross sections.

The top quark can decay at the tree-level into the new channels with final state particles consisting of up-type quarks (u or c) and a vector boson such Z boson through top FCNC interactions presented in Eq. (1.4). The top quark decay width Γ_t can be written as a summation of the SM decay widths plus the top quark decays originating from the top FCNC interactions with electroweak neutral gauge bosons. Thus, the top quark decay width Γ_t can be expressed as:

$$\Gamma t = \Gamma(t \longrightarrow W^+ b) + \Gamma(t \to W^+ s) + \Gamma(t \to W^+ d) + \Gamma(t \to cZ) + \Gamma(t \to uZ) + \Gamma(t \to c\gamma) + \Gamma(t \to u\gamma) \quad (1.5)$$

The predominant SM decay mode of the top quark is $t \to W^+b$, the decay width for this decay mode can be expressed as follows at the leading order (LO):

$$\Gamma(t \to W^+b) = \frac{\alpha |V_{tb}|^2}{16 s_W^2}\frac{m_t^3}{m_W^2}(1 - 3m_W^4/m_t^4 + 2m_W^6/m_t^6) \quad (1.6)$$

The expression of $\Gamma(t \to W^+b)$ the next to leading order (NLO) (33). The ratios of the SM decay widths are computed (34) as

$$\Gamma(t \to W^+s)/\Gamma(t \to W^+b) \simeq \frac{|V_{ts}|^2}{|V_{tb}|^2} \simeq 1.495 \times 10^{-3}$$

and $\Gamma(t \to W^+d)/\Gamma(t \to W^+b)\,\Gamma \simeq |V_{td}|^2/|V_{tb}|^2 \simeq 6.318 \times 10^{-5}$

The top quark FCNC decay width of the $t \to q\gamma$ channel, for $q = u, c$ is given as

$$\Gamma(t \to q\gamma) = \frac{\alpha}{4}(\lambda_{qL}^2 + \lambda_{qR}^2)\, m_t$$

Wile for the $t \to qZ$ channel, for $q = u, c$ can be expressed as (32)

$$\Gamma(t \to qZ) = \frac{\alpha\, m_t^3}{32 s_W^2 c_W^2 m_Z^2}(\kappa_{qL}^2 + \kappa_{qR}^2)(1 - m_Z^2/m_t^2)(2 - m_Z^2/m_t^2 - m_Z^4/m_t^4) \quad (1.7)$$

The estimations of the branching ratio of the decay mode t→qZ can be carried out using the relation:

$$BR(t \to qZ) = \frac{\Gamma(t \to qZ)}{\Gamma_t} \approx \frac{\Gamma\,(t \to qZ)}{\Gamma\,(t \to Wb)} \quad (1.8)$$

2. OVERVIEW OF THE COLLIDERS

Colliders serve a vital role in measuring various properties of subatomic particles and comprehending numerous phenomena related to them.They can be used as a probe for the internal structures of hadrons. This is anticipated to be achieved using future electron-hadron colliders (35). Collider technology has progressed from the first development of the charged particle colliders In recent years, it has advanced from being at the vanguard of advanced scientific equipment in high-energy physics and beam physics in the middle of the twentieth century.

In this chapter, we will review concisely the LHeC and FCC-he colliders related to the proposed study in this thesis. These colliders are designed as high-luminosity colliders and thus they are anticipated to provide great opportunities for accurate measurements at high energy scales.

2.1 Large hadron electron collider LHeC

The large hadron electron collider LHeC (36) collider has been proposed to expand the physics program by establishing collisions between electrons from one of the hadron beams from the LHC machine and a new accelerator infrastructure (37–38) (HL-LHC). It will permit TeV energy electron-proton collisions at a quit high luminosity, of O (10^{34}) cm^{-2} s^{-1}. In turn, this makes the LHeC collider a Higgs factory in addition to supporting new searches beyond SM physics (39). Moreover, it will enable the unraveling of the substructure of the matter and will contribute to the accuracy and discovery of physics at the HL-LHC and other future hadron colliders. In Fig 2.1, illustrates the schematic layout of the LHeC design based on an Energy Recovery Linac ERL, where each linac accelerates the beam to 10 GeV.The luminosity L for the LHeC can be evaluated from the relation (40)

$$L = \frac{N_e N_p \, n_p \mathfrak{f}_{rev} \gamma_p}{4\pi \epsilon_p \beta^*} \cdot \prod_{i=1}^{3} H_{i,} \qquad 2.1$$

Where $N_e = 10^9$ ($Np = 1.7 \cdot 10^{11}$) is the number of electrons (proton) per bunch, $\mathfrak{f}$ the revolution frequency, γ_P the relativistic factor E_P/M_P. In the above equation, $\epsilon_p = 3.7$ μm represents the normalized proton transverse beam emittance and $\beta^* = 0.1$m is the value of the proton beta function at the IP, expected to be equal in x and y. The luminosity is moderated by the hourglass factor, $H_1 = H_{geo} \simeq 0.9$, the pinch or beam-beam correction factor, $H_2 = H_{b-b} \simeq 1.3$, and the filling factor $H_3 = H_{coll} \simeq 0.8$, It should be noted that, the previously mentioned inputs parameters are taken from the conceptual design report CDR (40). These parameters are identical to the nominal LHC proton beam parameters and result in a peak luminosity of 10^{33} $cm^{-2}\,s^{-1}$ (41).

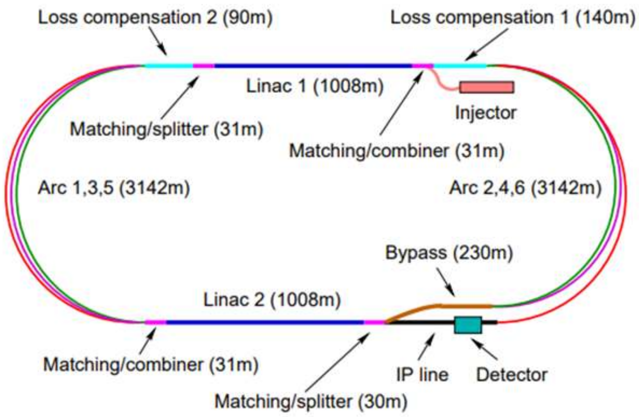

Figure 2.1. Schematic layout of the LHeC design based on an ERL. Each linac accelerates the beam to 10 GeV (42).

2.2 Future circular hadron electron collider FCC_he

Circular hadron colliders are characterized as discovery machines because their reach ability is dependent on beam energy. Thus, increasing the circumference of the LHC by factor 4 will result in a 100 TeV center of mass energy with a similar 16 T dipole (43). This in turn will allow for a much deep investigation of new physics at a high energy scale which is one of the objectives of the future circular colliders FCC.

The FCC collider is one of the planned high-energy frontier post-LHC colliders. It is planned to be built at CERN to increase the collision energy to 100 TeV. In the first stage of its construction, the FCC collider will be a luminosity-frontier highest-energy electron-positron (FCC-ee) collider. The stage then will be followed by the hadron collider (FCC-hh) and the future circular collider electron collider FCC-eh. In simultaneous operation, the FCC-eh collider is planned to operate for twenty-five years alongside the FCC-hh collider. This will yield an integrated luminosity equal to O (2) ab^{1}, at a nominal peak luminosity of more than 10^{34} cm^{2} s^{1}.

The FCC-eh (44) design allows reaching an integrated luminosity of 2 ab^{-1} and center of mass energy 3.5 TeV through colliding a 50 TeV proton beam with a 60 GeV (45) electron beam from a linear accelerator external and tangential to the main FCC tunnel. This collision is predictable to open a window to probe new physics in a way never done before.

The FCC-eh collider physics program will permit testing Higgs self-interactions, new physics models with extended Higgs sectors and dark matter proposed scenarios. Moreover, if neutrino oscillations are originated from the existence of heavy sterile neutrinos, direct searches at the FCC-eh may have an excellent finding potential in the kinematic regions complementary to the FCC-hh and FCC-ee. This makes the FCC complex a compelling candidate for highlighting the origin of neutrino masse (44).

3. AIM AND SCOPE OF THE STUDY

The essential target of this thesis is the investigation of the top quark FCNC in the process t → qZ. Particularly, we probe the tqZ couplings κ_{ut} and κ_{ct}, at the electron–proton future colliders namely, the LHeC and FCC-he planned ones. We plan to perform the study in the framework of effective field theory. Our goal is to obtain the best limits on the tqZ couplings via single top production in the $e\,p \rightarrow \nu_e\, Z\, q$ process, where Z boson eventually decays into $e^+e^-\ or\ \mu^+\mu^-$ or $q\bar{q}$ pairs. In the study, we also include the realistic detector effects by implementing Delphes in the Madgraph that is utilized in the generation of the signal and SM background events. For these generated events, we estimate the signal cross sections corresponding to the various couplings. In addition, we perform studies related to the kinematic distributions of the final states particles seeking the best cuts to be applied to improve the signal. Finally, we compute the statistical significance which allows us to extract the upper limits on the BR (t → qZ) where Z boson subsequently decays into ($\ell^+\ell^-$or $q\,\bar{q}$) at LHeC and FCC-he colliders with an integrated luminosity $1ab^{-1}$.

4. ANALYSIS AND RESULTS

In this chapter, we present our results and analysis related to the $e\ p \rightarrow \nu_e\ Z\ q$ process. The signal and background events, under concern in this study, are generated using Madgraph version MG5_aMC_V3_1_1 (46), where the effective Lagrangian for the signal was implemented via FeynRules (47). Next, the parton showering and realistic detector effects are executed with Pythia 6 (48), and Delphes 3.5.0 for LHeC and FCC-he (dedector) cards (49), respectively.

In section 4.1, we give a brief introduction about MadGraph. Then, in the rest of the sections of this chapter, analysis and results will be presented.

4.1 Madgraph

MadGraph 5 (50) is a very useful free source software for providing all the required elements for SM and BSM phenomenology. It is an automatic meta-code written in Python language that can be utilized in the generation of the tree-level and next-to-leading order Feynman diagrams of a given process. Besides, it can compute the tree-level and next-to-leading order cross sections, generate events for any process at colliders, of their matching to parton shower simulations, of merging matched samples that differ by light-parton multiplicities, as well as the usage of a number of instruments required for event editing and analysis MadGraph 5 includes many new, efficient algorithms that boost the performance and functionality of the program in all areas. In MadGraph 5 there is a new user interface, quite several new output formats, including C++ process libraries for Pythia 8 (51), and full compatibility with FeynRules for beyond SM physics implementation which allows for event generation for any model that can be expressed in Lagrangian format. All the capabilities of MadGraph enable avoiding the complexity of the calculations and the time wasting as well as performing the analysis of the given process within the SM and BSM in great precision

The procedure of implementing computation using MadGraph can be concisely described as follows: the first step is to specify a given process. This can be achieved through specifying the initial and final state particles and permitting a number of selected criteria that can involve, for instances, forced or forbidden s-channel resonances, not considered internal particles, and forced decay chains of final state particles. In the second step, multiparticle labels are used to pick out all possible processes that involve a range of particles. Therefore, MadGraph produces all Feynman diagrams for the process. In fact, MadGraph generates a visual representation of the produced Feynman diagrams for the process. In addition, MadGraph constructs the computer code necessary to evaluate the matrix element at a given point in the phase space. In the third step, the evaluation of the matrix elements can be done through calls to helicity wave functions and amplitudes, as were first implemented in the HELAS package (52). This operation is effective as it clearly allows helicity wave functions corresponding to similar subdiagrams to be reused across diagrams. In the fourth step, the computer code generated by MadGraph can be used to generate events and estimate cross-section or decay width, for instance, with the help of the MadEvent package (53).

The evaluation of the cross-section using MadGraph includes three stages: generation, output, and running. Each stage is achieved by implementing on-line commands in the MadGraph shell. The commands can be accessed through the execution from a terminal shell in the main directory. Examples of these commands and their descriptions are given below.

When "/bin/mg5 aMC " command is written in the command line in the terminal, one can go inside the Madgraph with a prompt showing "MG5 aMC>". The three stages, of the evaluation of the cross-section, mentioned above are realized by the following three commands in the MadGraph shell: "generate", "output", and "launch". After generating the process, the parameters related to the run will be stored in different cards (inside the Cards directory). Some of the important cards used are listed below with a brief explanation:

param_card: this card includes all the parameters of the model such as masses, couplings,

run_card: all the parameters in relation to the collider and run settings including energy, Nevents, cuts, scales can be found this card.

pythia_card (MadEvent) / shower_card (aMC): parameters in needs to shower the partonic events

plot_card (MadEvent): which variables to plot

delphes/pgs_card: simulation for detector response

Having briefly discussed MadGraph, we are ready now to perform the required calculations for the process $ep \to \nu_e\, Z\, q$ followed by various Z boson decay channels at LHeC and FCC-he using the effective field theory approach. The process can be generated using MadGraph5 through executing the following command:

MG5aMC> generate $ep \to \nu_e\, Z\, q$.

For the process under concern in this thesis, the inclusion of the model expressed by the Lagrangian given in Eqs. (1.4) in MadGraph5_aMC@NLO can be done using FeynRules package (46) as a Universal FeynRules Output (UFO) (54). After implementation of this UFO model file in MadGraph5_aMC@NLO, one can directly estimate the cross sections of the processes $ep \to \nu_e\, Z\, q \to \nu_e\, q\ell\ell$ and $ep \to \nu_e\, Z\, q \to \nu_e\, q\, \bar{q}q$ at the future LHeC and FCC-he colliders at different center of mass energies. Example of shell script (KappaLRuZero_KappaLRcvarry.sh.) used in MadGraph5_aMC@NLO to scan the couplings (for production cross section) between $K_{ut} = 0$ to $K_{ut} = 0.1$ and $K_{ct} = 0$ to $K_{ct} = 0.1$ for LHeC collider is given in Figure 4.1. The name of the model is top FCNC which has been discussed in details in chapter 2. Below, we give descriptions to a set of essential commands listed in Figure 4.1.

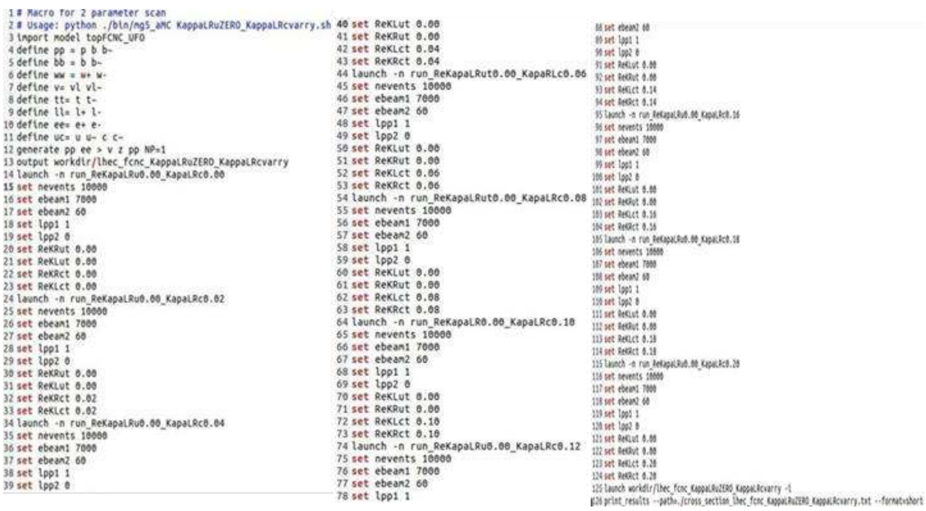

Figure 4.1. Section of Shell script (*KappaLRuZero_KappaLRcvarry.sh*) to scan κ_q coupling where $\kappa_{ut} = \kappa_{ct}$.

4.2 Cross-section for the process e p → ν_e Z q

The results for the total cross sections of the process e p → υ_e Z q, where q might be up or charm quark, are given in this section. These cross sections will be displayed for various values of the couplings K_q and can shed light on the top quark anomalous FCNC interactions in the tqZ vertices.

There are three cases shown in Figure 4.2 for the process e p → υ_e Z q at LHeC future collider. First case, both κ_{ut} and κ_{ct} set equal to each other and then varied between 0 and 0.2. In the second case, we take $\kappa_{ut} = 0$ and vary κ_{ct} in the range [0, 0.2]. The third case corresponds to setting $\kappa_{ct} =0$ and varying $\kappa_{ut} = \kappa_{ct}$ in the range [0, 0.2]. The cross sections in the presence of FCNC are evaluated for these values and plotted in the left plot of the figure in blue, red, and black colors for the first case, second case and third case respectively. This figure shows that the cross section for $\kappa_{ut} = \kappa_{ct} =0$ is 0.74 pb (which is SM) and increases up to the 1.08 pb as we see from blue line. On the other hand, in Figure 4.2 right, we show the two-dimensional density plot of the total cross-section as a function of the two couplings κ_q where the colors indicate the values of the cross sections, we used the fit function in our computation:

$$\sigma\,(\kappa_{ut}, \kappa_{ct}) = a\,{\kappa_{ut}}^2 + b\,{\kappa_{ct}}^2 + c\,\kappa_{ut}\,\kappa_{ct} + d$$

Where a = 0.126098, b = 1.06332, c = 0.122115, and d = 0.529004.

We also note from the left plot in the Figure that larger cross section can be obtained for the first case $\kappa_{ut} = \kappa_{ct}$ with non-vanishing values of the couplings. Moreover, the cross sections for the second and third case in which one of the couplings is zero and the other is not equal to zero have very close values. Deviations of the cross-section start to appear at approximately 0.02 for all three considered cases for the couplings. These deviations indicate that the cross section is enhanced for the case $\kappa_{ut} = \kappa_{ct}$. Regarding the right plot in Figure 4.2, we remark the dependence of the cross section simultaneously on the couplings κ_{ut} and κ_{ct} where colors indicate the strength. The cross-section increases remarkably, as can be noted from the yellow color in the plot, at large values of the couplings.

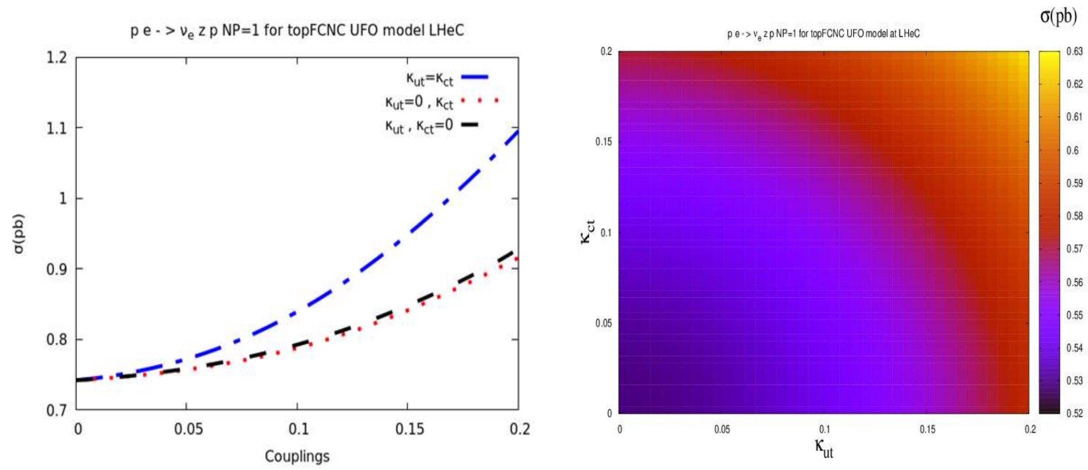

Figure 4.2. Left: the cross-section for the e p → ν_e Z q process including the anomalous FCNC tq Z vertex as a function of the couplings κ_{ut} and κ_{ct} at LHeC future collider. The right plot represents the two-dimensional density plot of the cross-section at the same collider.

In Figure 4.3 we display the plots corresponding to the three aforementioned cases in Figure 4.2. Following similar discussions to the one done in Figure 4.2, we see from the left plot of the Figure that, the SM prediction of the cross-section is 2 pb and enhanced to roughly 2.8 pb in the presence of the non-vanishing couplings κ_{ut}=κ_{ct}. Therefore, in this case, the cross-section can be increased with respect to the SM by a value up to 50 %. In the right plot, Figure 4.3, we varied both κ_{ut} and κ_{ct}, noticeably, large values of the couplings $\kappa_{ut}$and κ_{ct} result in an increment in the cross-section as demonstrated by the yellow color. It should be remarked that, for obtaining the right plot, the fit function is written as:

$$\sigma(K_{ut}, K_{ct}) = a\, {K_{ut}}^2 + b\, {K_{ct}}^2 + c\, K_{ut}\, K_{ct} + d$$

Where a = 9.58073, b = 8.3631, c = 0.563768, and d = 2.31374.

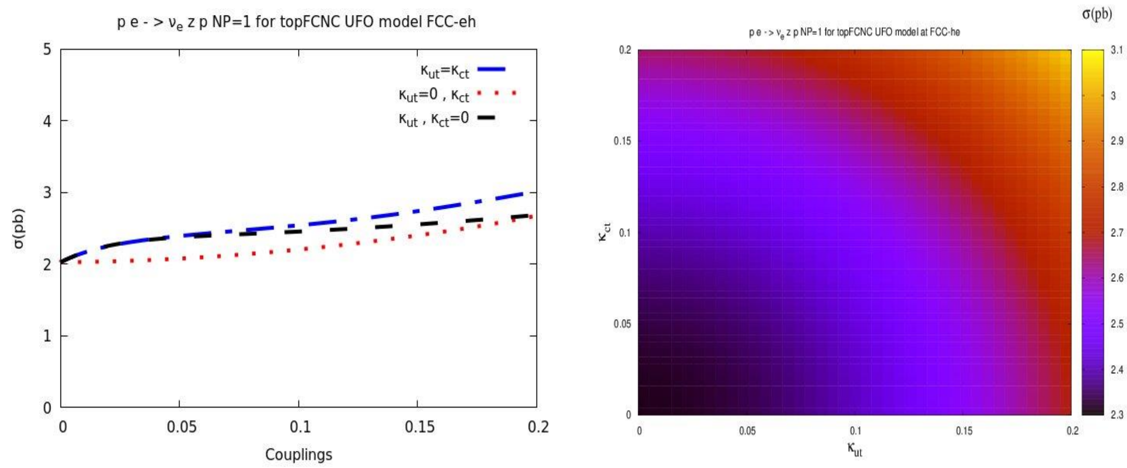

Figure 4.3. Left: the cross-section for the e p → ν_e Z q procses including the anomalous FCNC tqZ vertex as a function of the couplings κ_{ct} and κ_{ut} at FCC-he future collider. The right plot denotes the two-dimensional density plot of the cross-section at the same collider.

4.3 Kinematic distribution of final state particles at LHeC future collider

This section elaborates the kinematic variables of the final state particles at LHeC future collider. In particular, we consider the transverse momentum P^T, pseudo rapidity η, missing transverse energy MET, and invariant mass of the Z boson reconstructed from leading and sub leading light charged leptons with opposite electric charges or the leading and sub leading jets according to the final state particles.

In order to reveal the distribution of kinematic variables of final state particles, we prouduce all graphs of the signal and SM background with the same final state particles using madgraph, Pythia and Delphes procedure as mentioned before. Distributions are examined in the following sections where the singly produced Z boson decays to $e^+ e^-$ or $\mu^+ \mu^- or\ q\bar{q}$.

4.3.1 e p → ν_e Z q → ν_e $e^+ e^-$ *q*

In this channel, the produced top quark decays through FCNC into Z boson and q quark, i.e. t → Zq → q e^+e^- . In the figures starting from Figure 4.4 till figure 4.8, we present our results corresponding to the LHeC future collider with integrated luminosity 1 ab^{-1} and for chosen values of the couplings taken as κ_{ut}=κ_{ct} = 0.3, where the red curve represents the SM background while the blue curve points out to the signal.

Figure 4.4, exhibits the kinematic distributions of the transverse momentum of leading electron $P_{e_1}^T$ (top left), pseudo-rapidity η_{e_1}(top right), $cos\theta_{e_1}$(bottom left) and the azimuthal angle ϕ_{e_1} (bottom right) corresponding to the process under concern. Regarding the distributions in the top left and right plots, we note that the signal is enhanced much larger compared to the SM for the value of the $P_{e_1}^T$ below [60 GeV], and for the η_{e_1} in the range [3,5]. Diverting now to the bottom left plot in the figure, we find that values of $cos\theta_{e_1}$ close to one lead to maximum enhancements in the signal. Concerning the azimuthal angle ϕ_{e_1}, one can see from the plot in the bottom right of the figure that, the signal is boosted compared to the background for all values of the ϕ_{e_1}.

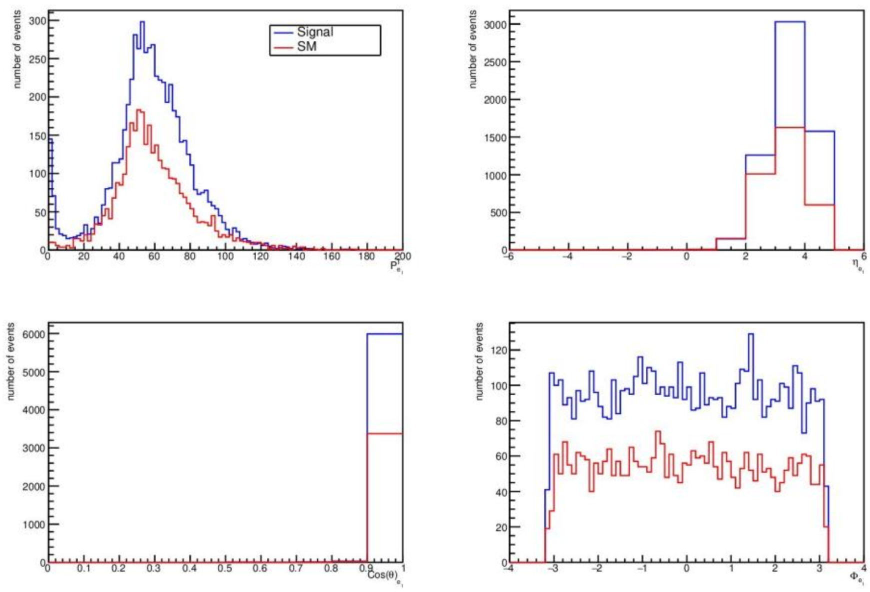

Figure 4.4. The distributions of the transverse momentum of the leading electron $P_{e_1}^T$ (top left), pseudo-rapidity η_{e_1} (top right), $cos\theta_{e_1}$(bottom left) and the azimuthal angle ϕ_{e_1} (bottom right) for the process e p → ν_e Z q → ν_e e^+ e^- q at the LHeC collider for a chosen values $\kappa_{ut} = \kappa_{ct} = 0.3$.

Figure 4.5, has plots of the same distributions presented in Figure 4.4 but here they correspond to subleading electron for the same process. Clearly from the left plot in the same Figure, a large enhancement in the signal compared to the SM occurs at values of the transverse momentum of sub leading electron $P_{e_2}^T$ lay in the interval [20 GeV,40 GeV]. Additionally, from the top right plot, we see that the signal is enhanced considerably in comparison with the SM for values of pseudo-rapidity η_{e_2} in the interval [2,5].

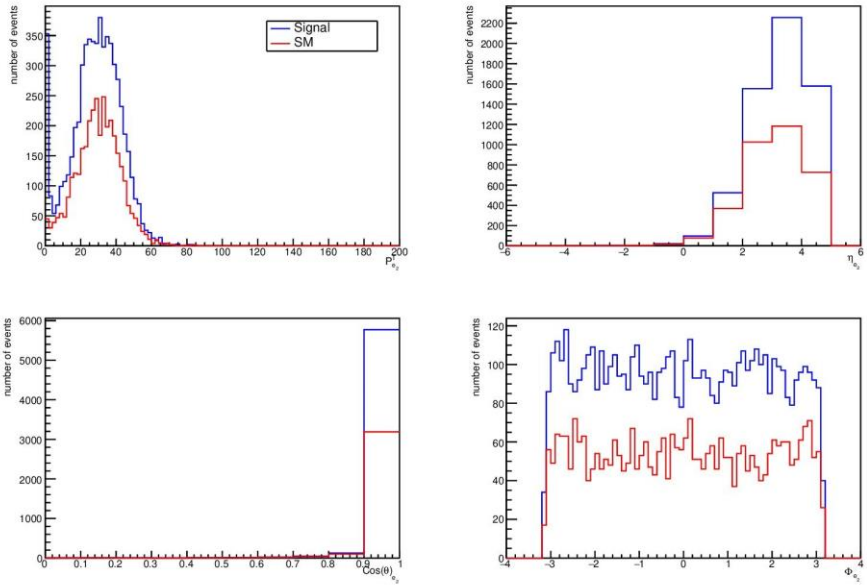

Figure 4.5. The distributions of the transverse momentum of sub leading electron $P^T_{e_2}$ (top left), pseudo-rapidity η_{e_2} (top right), cos θ_{e_2} (bottom left) and the azimuthal angle ϕ_{e_2}(bottom right) corresponding to the process e p → ν_e Z q → ν_e e^+ e^- q at the LHeC collider for a chosen values $\kappa_{ut} = \kappa_{ct}$= 0.3.

The kinematic distributions of the quark produced in the process e p → υ_e Z q → υ_e e^+e^-q**,** are shown in Figure 4.6. From the top left plot, we deduce that signal can be enhanced much larger compared to the SM for values of the transverse momentum $P^T_{q_1}$ belong to the interval [30 GeV,70 GeV]. Moreover, from the top right plot, one can notice that, the signal is largely enhanced comparing to the SM one when the pseudo-rapidity takes values roughly in the range [2,5]. From the bottom left (right) plots in the same Figure, the large enhancements in the signal correspond to large values of cosθ_{q_1}close to one and to all the azimuthal angle ϕ_{q_1}.

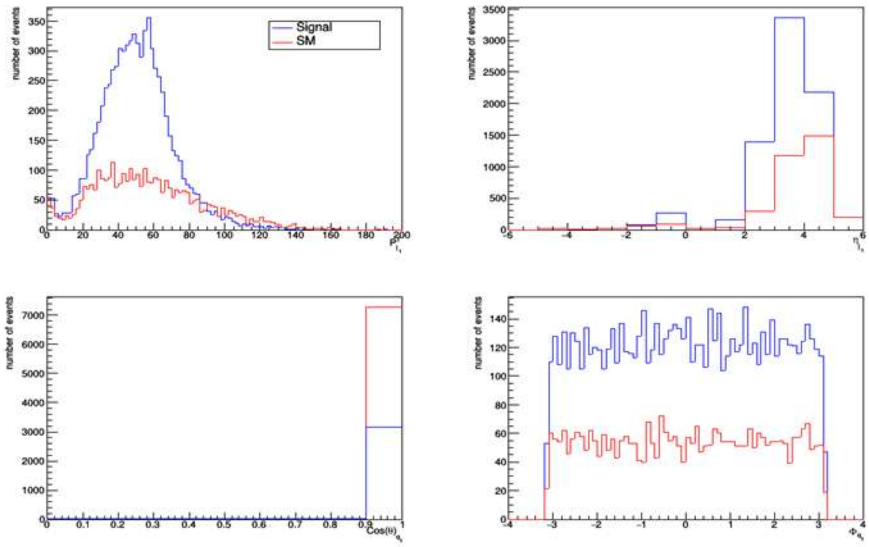

Figure 4.6. The distributions of the transverse momentum $P^{T}_{q_1}$ (top left), pseudo-rapidity η_{q_1} (top right), cos θ_{q_1} (bottom left) and the azimuthal angle ϕ_{q_1} (bottom right) of the quark corresponding to the process e p → ν_e Z q → ν_e e^+ e^- q at the LHeC collider for a chosen values $\kappa_{ut} = \kappa_{ct} = 0.3$.

The distributions of the angular distances between the final state particles e_1, e_2 and q_1, ΔR_{e1e2} (top left), $\Delta R_{e_1 q_1}$(top right), $\Delta R_{e_2 q_1}$(bottom left), and the Missing Transverse Energy MET (top right) are shown in Figure 4.7. The angular separation $\Delta R_{1,2}$ is evaluted as $\Delta R_{1,2} = \sqrt{(\eta_1 - \eta_2)^2 + (\phi_1 - \phi_2)^2}$ between the two final particles.

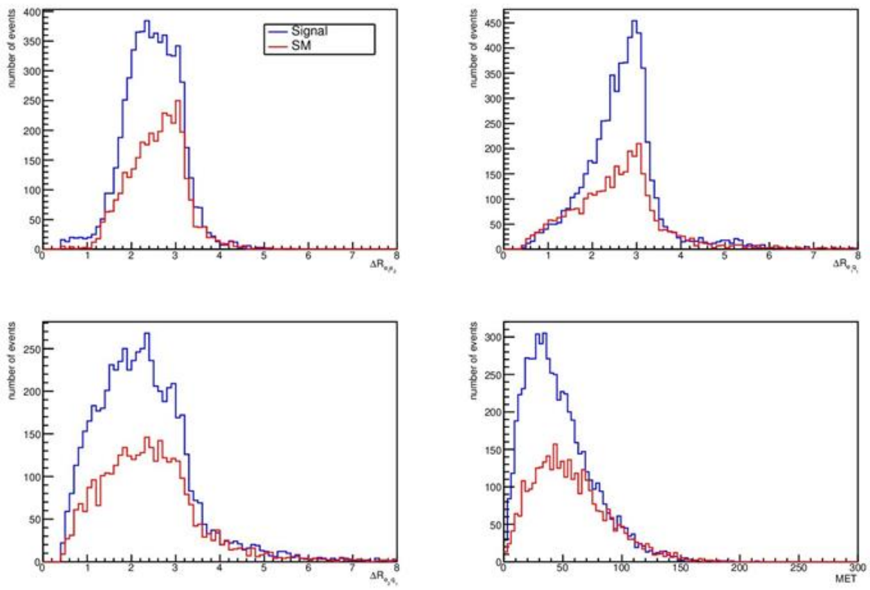

Figure 4.7. The distributions of the angular separation particles: leading electron $\Delta R_{e_1e_2}$(top left), leading electron and quark $\Delta R_{e_1q_1}$(top right), subleading electron and quark $\Delta R_{e_2q_1}$ (bottom left), as well as MET (bottom lright) for the process e p → ν_e Z q → ν_e e^+ e^- q at the LHeC collider for a chosen values $\kappa_{ut} = \kappa_{ct} = 0.3$.

In Figure 4.8, we demonstrate the kinematic distributions of both signal and SM of the invariant mass of the Z boson reconstructed from the two electrons $M_{e_1e_2}$(left) and the invariant mass of $M_{e_1e_2q_1}$(right) where we require that the reconstructed mass of two electrons lies between 86 GeV < $M_{e_1e_2}$ < 92 GeV. Clearly from the left plot in the figure, the signal has a peak around the Z mass and is larger than the SM. On the other hand, and from the right plot in the figure, the peak of the signal is shifted around invariant mass $M_{e_1e_2q_1}$=150 GeV approximately and becomes much larger than the SM background.

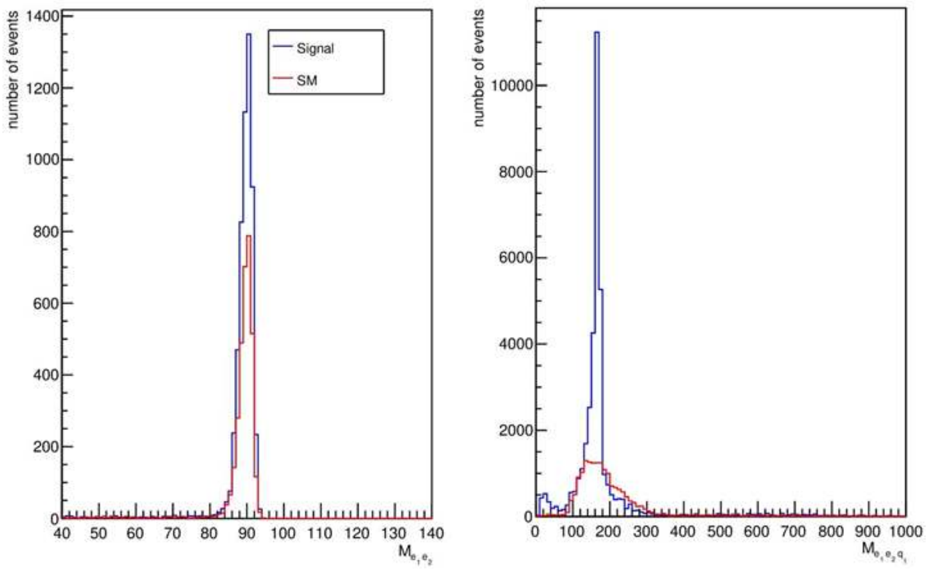

Figure 4.8. Invariant mass distribution of Z boson for two electrons $M_{e_1 e_2}$(left) while the right plot includes the invariant mass of Z boson with one quark $M_{e_1 e_2 q_1}$ at LHeC.

4.3.2 $e\, p \rightarrow \nu_e\, Z\, q \rightarrow \nu_e\, \mu^+ \mu^-\, q$

In this process, the generated top quark decays to a Z boson and light q quark, then followed by decaying of the Z boson into muon anti-muon pair $t \rightarrow Zq \rightarrow \mu^+ \mu^- q$. In the figures below, we display our results for the case of the LHeC future collider with integrated luminosity 1 ab^{-1}. In this channel, we take the values of the couplings as $\kappa_{ut} = \kappa_{ct} = 0.7$ to evaluate the kinematic distributions of the final state particles for SM background and signal.

Figure 4.9, illustrates the kinematic distributions which are represented as the transverse momentum of leading muon $P^T_{\mu 1}$ (top left), pseudo-rapidity η_{μ_1} (top right), cos θ_{μ_1} (bottom left) and the azimuthal angle ϕ_{μ_1} (bottom right) corresponding to the process $e\, p \rightarrow \upsilon_e\, Z\, q \rightarrow \upsilon_e\, \mu^+ \mu^- q$. One can remark from the plots in the figure that, the distributions concerning this process follow same behavior as in the process $e\, p \rightarrow \upsilon_e\, Z\, q \rightarrow \upsilon_e\, e^+ e^- q$ with little bit differences where the signal here is enhanced much larger compared to the SM for value of the

$P^T_{\mu 1}$ and η_{μ_1} lies in the range [50 GeV,90 GeV] and [3,4], respectively. Moreover, the enhancements in the signal is achieved at values of cos θ_{μ_1} close to one.

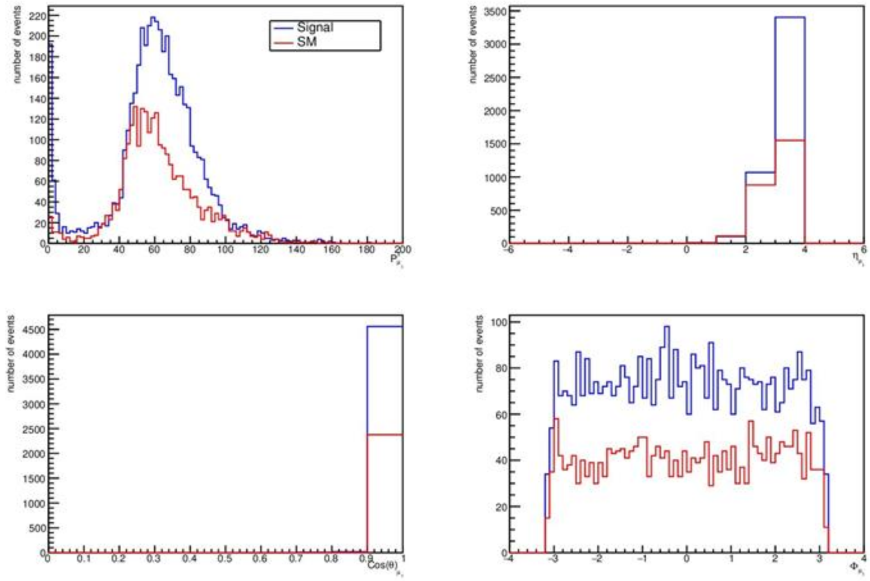

Figure 4.9. The distributions of the transverse momentum of leading muon $P^T_{\mu 1}$ (top left), pseudo-rapidity η_{μ_1} (top right), cos θ_{μ_1} (bottom left) and the azimuthal angle ϕ_{μ_1} (bottom right)) corresponding to the process e p → ν_e Z q → ν_e $\mu^+\mu^-$ q at the LHeC collider for a chosen values κ_{ut}= κ_{ct}= 0.7.

We consider now the same kinematic distributions for the subleading muon. These distributions with K_{ut}=K_{ct} = 0.7 are displayed in Figure 4.10 for the same process e p → υ_e Z q → υ_e $\mu^+ \mu^- q$. Again, the plots show same patterns as in Figure 4.9 However, the large values of the signal compared to the SM background occur at values of the $P^T_{\mu 2}$ and pseudo-rapidity roughly belong to the intervals [25 GeV,45 GeV] and [2,4] respectively. Another remark from the bottom plots is that, the improvements in the signal can be obtained at values of cos θ_{μ_2} close to one and for all values of the azimuthal angle ϕ_{μ_2} which was the case also in the previous cases.

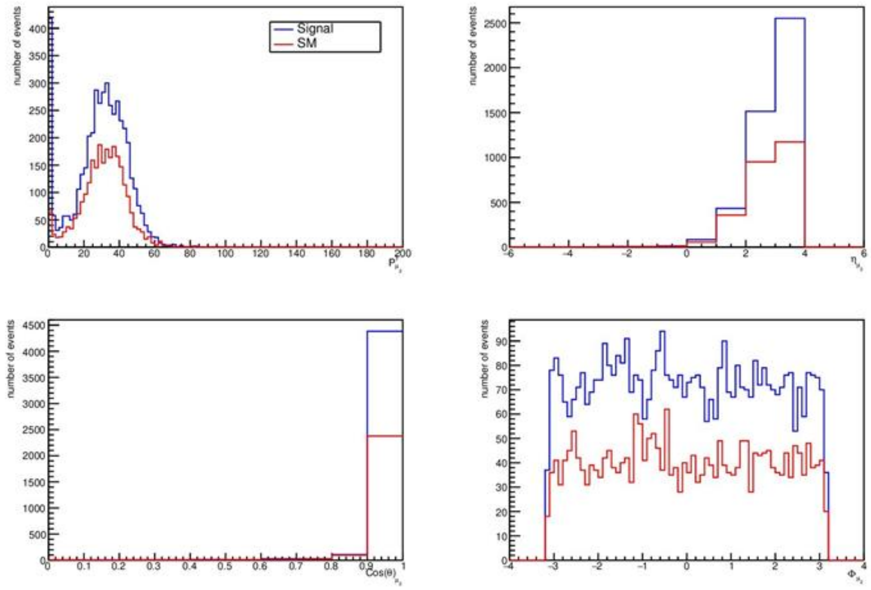

Figure 4.10. The distributions of the transverse momentum subleading muon $P^T_{\mu 2}$ (top left), pseudo-rapidity η_{μ_2}(top right), cos θ_{μ_2}(bottom left) and the azimuthal angle ϕ_{μ_2} (bottom right) corresponding to the process e p → ν_e Z q → ν_e $\mu^+\mu^-$ q at the LHeC collider for a chosen values κ_{ut}= κ_{ct}= 0.7.

We divert now to discuss the kinematic distributions of the quark in the decay channel e p → υ_e Z q → υ_e μ^+ μ^-q, they are shown in Figure 4.11. One can see from the figure that, the signal is notably enhanced compared to the SM for P^T_{q1} lies in the range [30 GeV,70 GeV] and η_{q_1} roughly in the range [2,5]. On the other hand, from the same figure, larger raises in the signal can be obtained for cos θ_{q_1} close to one.

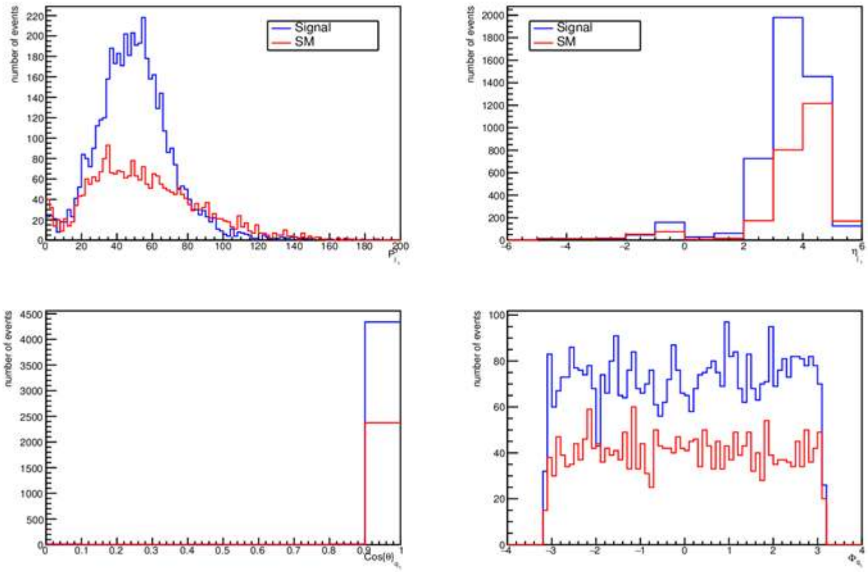

Figure 4.11. The distributions of the transverse momentum P_{q1}^{T} (top left), pseudo-rapidity η_{q_1}(top right), cos θ_{q_1}(bottom left) and the azimuthal angle ϕ_{q_1}(bottom right) of the quark corresponding to the process e p → ν_e Z q → ν_e $\mu^+\mu^-$ q at the LHeC collider for a chosen values κ_{ut}= κ_{ct}= 0.7.

In Figure 4.12, The distributions of the angular distances between the final state μ_1, μ_2 and $q_{1,}$ where $\Delta R_{\mu_1,\mu_2}$ (top left), $\Delta R_{q_1\mu_1}$(top right), $\Delta R_{q_1\mu_2}$ (bottom left) as well as the Missing Transverse Energy MET (top right) are presented for the effective couplings K_{ut}=K_{ct} = 0.7 at LHeC.

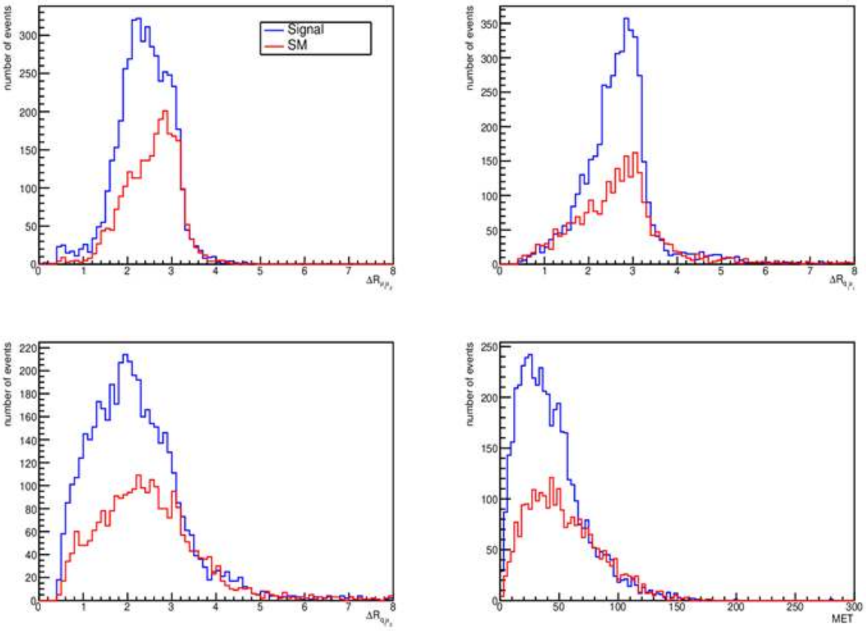

Figure 4.12. The distributions of the the angular separation particles: top left $\Delta R_{\mu_1,\mu_2}$, top right $\Delta R_{q_1\mu_1}$bottom left $\Delta R_{q_1\mu_2,}$ as well as the MET (bottom right) at LHeC collider.

Figure 4.13, clarifies the kinematic distributions of both signal and SM of the invariant mass of the Z boson reconstructed from the two muons $M_{\mu_1\mu_2}$ (left) and the invariant mass $M_{\mu_1\mu_2q_1}$(right) where we require that the reconstructed mass of two muons lies between 86 GeV < $M_{\mu1\mu2}$ < 92 GeV. Plainly, from the left plot in the figure, the signal has a peak around the Z mass and is larger than the SM background. Furthermore, from the right plot in the figure, the peak of the signal corresponds to invariant mass $M_{\mu_1\mu_2q_1} = 170$ GeV.

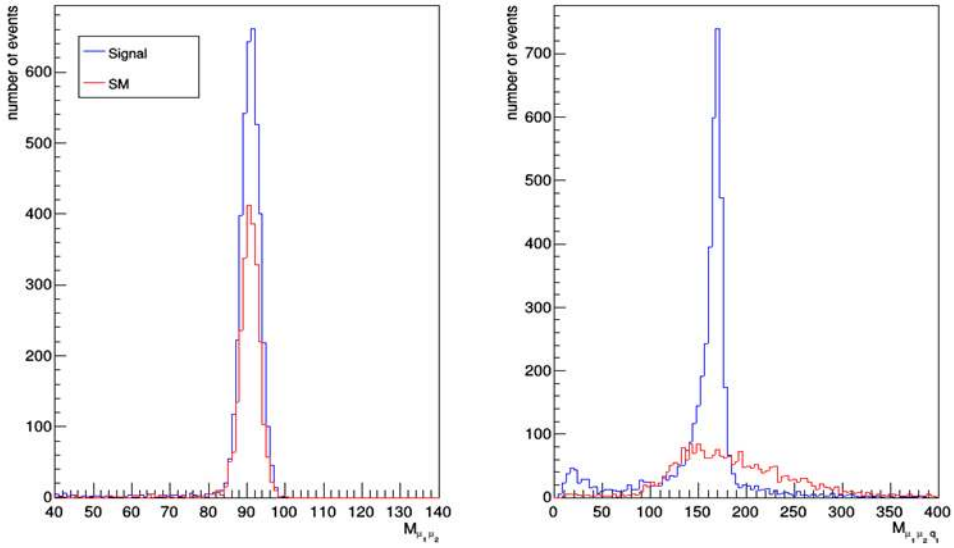

Figure 4.13. Invariant mass distributions of Z boson (left-handed) for muon while the(right-handed) includes the invariant mass for two muons with one quark $M_{\mu_1\mu_2q_1}$ for the signal and background at LHeC.

4.3.3 e p → ν_e Z q → ν_e q $\bar{q}$ q

In addition to the previous channels, we consider the process where the produced top quark decays to Z boson and q quark. We are interested here in the process $t \rightarrow$ Zq $\rightarrow q\,\bar{q}q$ at LHeC future collider with integrated luminosity 1 ab^{-1}. In this process, we choose the values of the couplings as $\kappa_{ut} = \kappa_{ct}$= 0.1 to estimate the kinematic distributions of the final state particles for both signal and SM background.

In Figure 4.14, we illustrate the kinematic distributions for the transverse momentum of the leading jet $P_{j_1}^T$ (top left), the pseudo-rapidity η_{j_1} (top right), cos θ_{j_1} (bottom left) and the azimuthal angle ϕ_{j_1} (bottom right). Analogous to the distributions in the processes e p → υ_e Z q → υ_e e^+e^-q and e p → υ_e Z q → υ_e $\mu^+\mu^-q$, we recognize from all these distributions that the signal (in the blue curve) is larger in a comparison with SM background (red curve) for values $P_{j_1}^T$, η_{j_1}, lay in the ranges [30 GeV,80 GeV] and [3,5] respectively. Moreover, the enhancements in the signal take place for values of cos θ close to one.

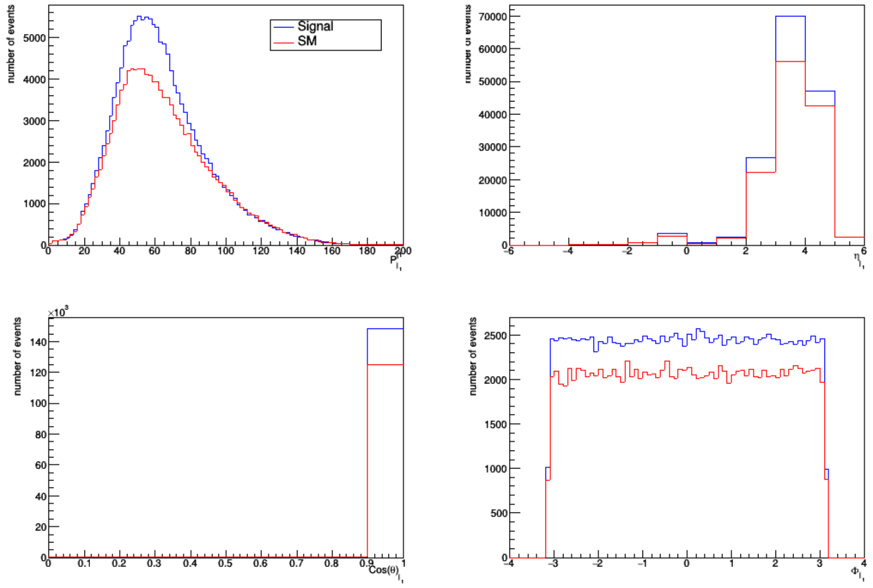

Figure 4.14. The distributions of the transverse momentum of the leading jet $P^T_{j_1}$ (top left), pseudo-rapidity η_{j_1} (top right), cos θ_{j_1} (bottom left) and the azimuthal angle ϕ_{j_1} (bottom right) corresponding to the process e p → ν_e Z q → ν_e q $\bar{q}$ q at the LHeC collider for a chosen values κ_{ut}= κ_{ct}= 0.1.

Considering the subleading jet, in Figure 4.15 we plot of the same distributions presented in Figure 4.14 for the same process. Distinctly, from the left plot in the figure that, a large enhancement in the signal compared to the SM occurs at values of the $P^T_{j_2}$ lay in the interval [0 GeV, 60 GeV]. Furthermore, from the top right plot, we deduce that the signal is enhanced considerably in comparison with the SM for values of η_{j_2} in the interval [2, 5].

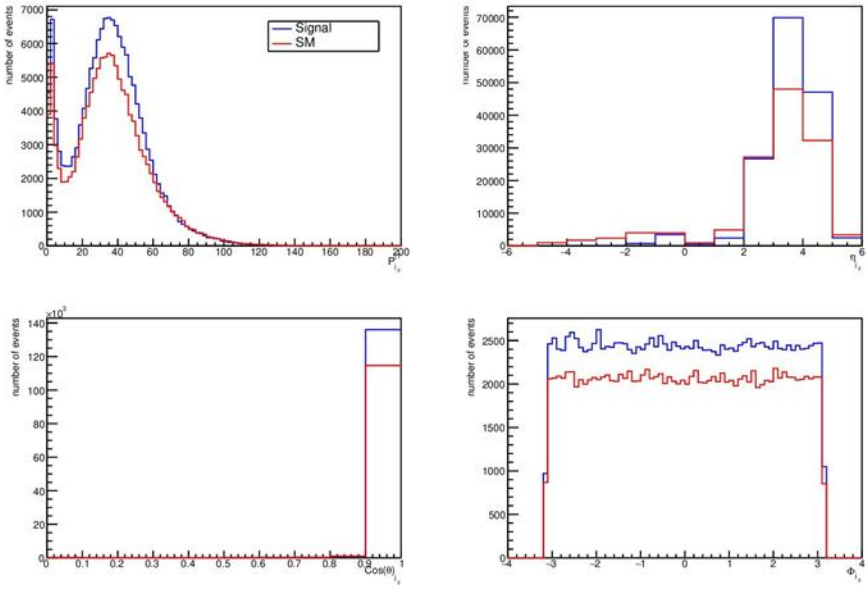

Figure 4.15. The distributions of the transverse momentum of subleading jet, $P_{j_2}^T$ (top left), pseudo-rapidity η_{j_2} (top right), cos θ_{j_2} (bottom right) of the subleading jet corresponding to the process e p → ν_e Z q → ν_e q $\overline{\text{q}}$ q at the LHeC collider for a chosen values $\kappa_{ut} = \kappa_{ct}$ = 0.1.

We discuss now the kinematic distributions of the quark produced in the process e p → υ_e Z q → υ_e q $\overline{\text{q}}$q, where distributions in this case are shown in Figure 4.16. From the top left plot, the transverse momentum P_{q1}^T in the range [0 GeV, 30 GeV]. Additionally, from the top right plot, the enhancement can be obtained when the pseudo-rapidity η_{q_1} takes values roughly in the range [2, 5]. Similar to all previous studied cases, values of cos θ_{q_1}close to one lead to large signal and this is the conclusion also for all values of the azimuthal angle ϕ_{q_1}.

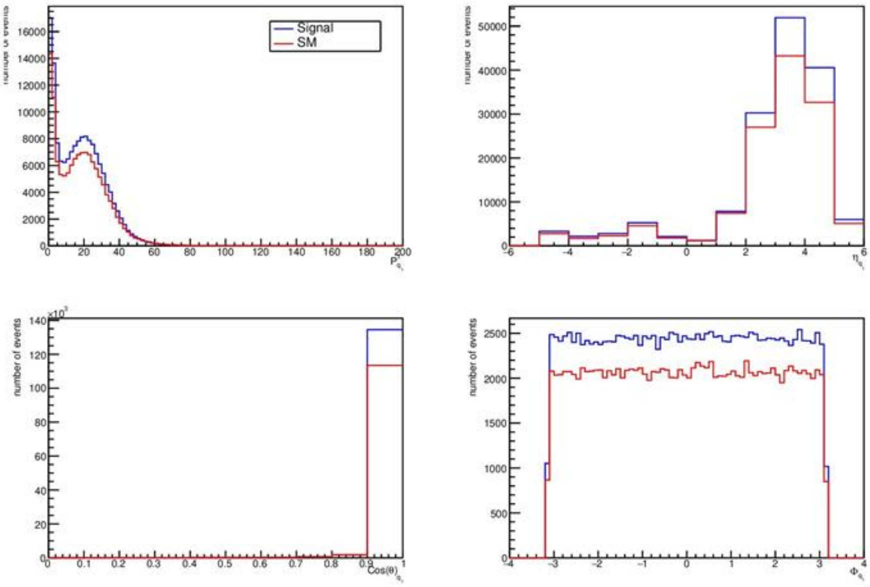

Figure 4.16. The distributions of the transverse momentum P_{q1}^{T} (top left), pseudo-rapidity η_{q_1}(top right), cos θ_{q_1}(bottom left) and the azimuthal angle ϕ_{q_1}(bottom right) of the quark to the process e p → ν_e Z q → ν_e q $\bar{q}$ q at the LHeC collider for a chosen values κ_{ut}= κ_{ct} = 0.1.

The distributions of the angular distances of the leading jet $\Delta R_{j_1 j_2}$ (top left), subleading jet $\Delta R_{j_1 q_1}$(top right), $\Delta R_{j_2 q_1}$ (bottom left), as well as missing transverse energy MET (bottom right) are illustrated in Figure 4.17.

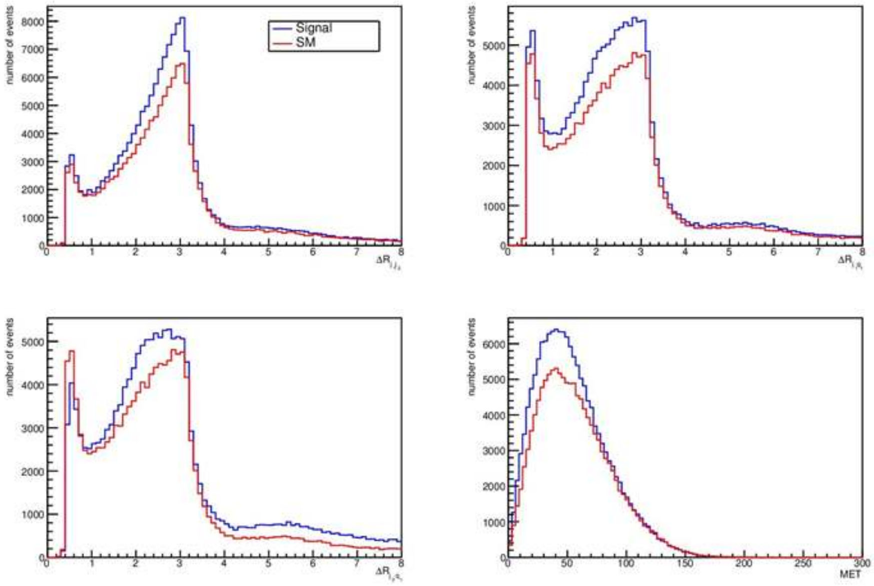

Figure 4.17. The angular separation top left $\Delta R_{j_1 j_2}$, top right $\Delta R_{j_1 q_1}$, bottom left $\Delta R_{j_2 q_1}$ and bottom right represents MET, at LHeC collider.

In Figure 4.18, we show The distributions of the invariant masses of the Z boson reconstructed of the two jets, are displayed for both the signal and the SM left and right respectively. In this figure we demand that the reconstructed mass of the two jets fall in the range of 86 GeV$< M_{j_1 j_2} <$ 92 GeV. The signal has a peak around the Z mass and is larger than the SM background, which is evident from the left plot in the figure. The peak of the signal, on the other hand, is displaced around invariant mass $M_{j_1 j_2 q_1}$ = 150 GeV.

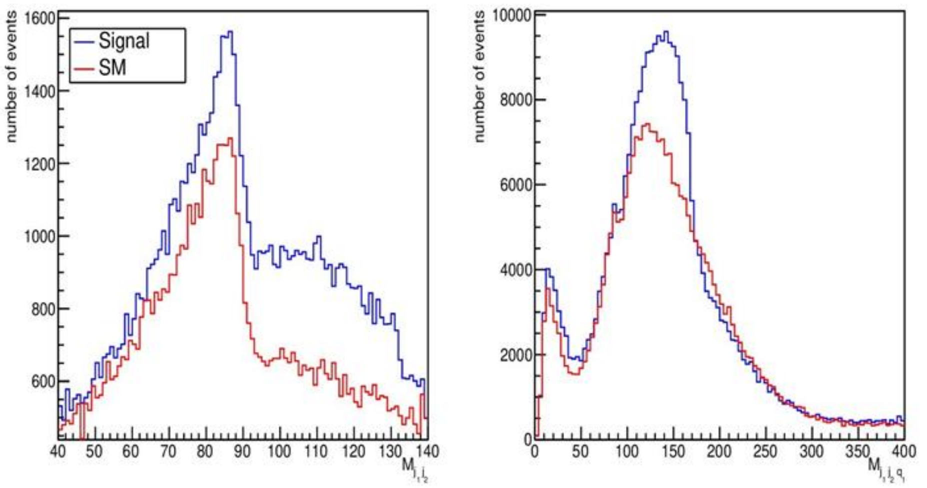

Figure 4.18. Invariant mass distributions of Z boson (left) of jets $M_{j_1 j_2}$ while the (right) includes the invariant mass for two jet with one quark $M_{j_1 j_2 q_1}$ for the signal and background at LHeC.

4.4 Kinematic distribution of final state particles at FCC-he future collider

In this part , we investigate the kinematic variables of the final state particles at FCC-he future collider with integrated luminosity 1 ab^{-1} in a similar way to what was done in the previous section. Consequently, these variables are P^T, η, MET, and invariant mass of the Z boson reconstructed from leading and sub leading light charged leptons with opposite electric charges or the leading and sub leading jets depending on the final state particles. In addition, we give details of the simulation and the cut-based analysis steps in order to separate signal from background. In all figures, the red curve represents the SM while the signal is depicted by the blue curve.

4.4.1 e p → ν_e Z q → ν_e e^+ e^- q

We start with the FCNC top quark decay $t \rightarrow$ Zq → q e^+e^- , we present our plots concerning the distributions of the kinematic variables for the FCC-he future collider with integrated luminosity 1ab^{-1} and for particular coupling values taken as K_{ut}=K_{ct} = 0.1.

Figure 4.19, displays the kinematic distributions of the leading electron for both signal and SM background corresponding to the process e p → υ_e Z q → υ_e e^+e^-q. The plots are as follows: transverse momentum of leading electron $P_{e_1}^T$

(top left), pseudo-rapidity η_{e_1} (top right), $cos\theta_{e_1}$ (bottom left) and the azimuthal angle ϕ_{e_1} (bottom right). Concerning the distributions in the figure, we barely can discriminate the signal from SM unlike the distributions in the case of the LHeC collider in which signal and SM can be distinguished.

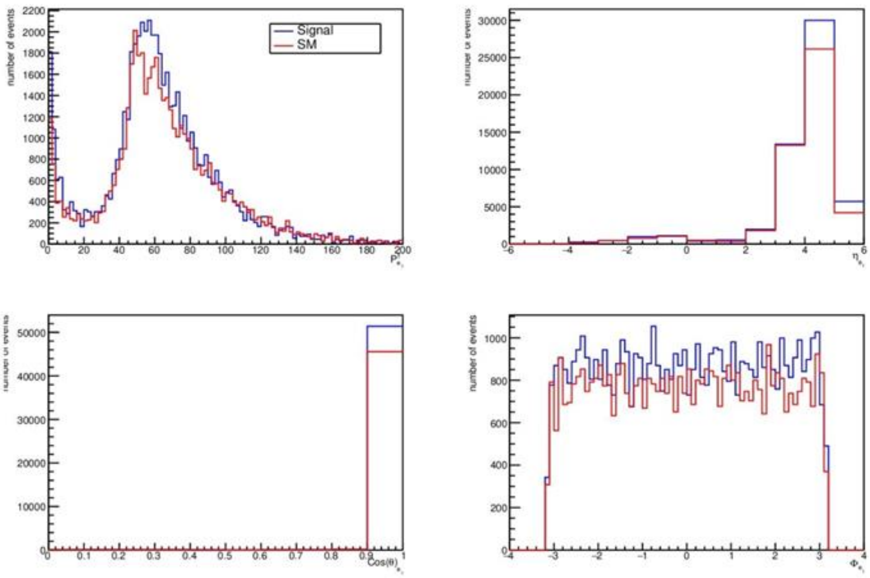

Figure 4.19. The distributions of the transverse momentum of leading electron $P_{e_1}^{T}$ (top left), pseudo-rapidity η_{e_1} (top right), $cos\theta_{e_1}$ (bottom left) and the azimuthal angle ϕ_{e_1}(bottom right) corresponding to the process e p → ν_e Z q → ν_e e^+ e^- q at the FCC-he collider for a chosen values $\kappa_{ut} = \kappa_{ct}$= 0.1.

The distributions plotted in Figure 4.20 correspond to the transverse momentum of sub leading electron $P_{e_2}^{T}$. From the left top we barely can distinguish the signal from the SM,this is contrary to the previous collider LHeC where all the distributions can be observed readily. The other plots of the pseudo-rapidity, cos θ_{e_2} and the azimuthal angle ϕ_{e_2} indicate also that signal and background follow same behavior.

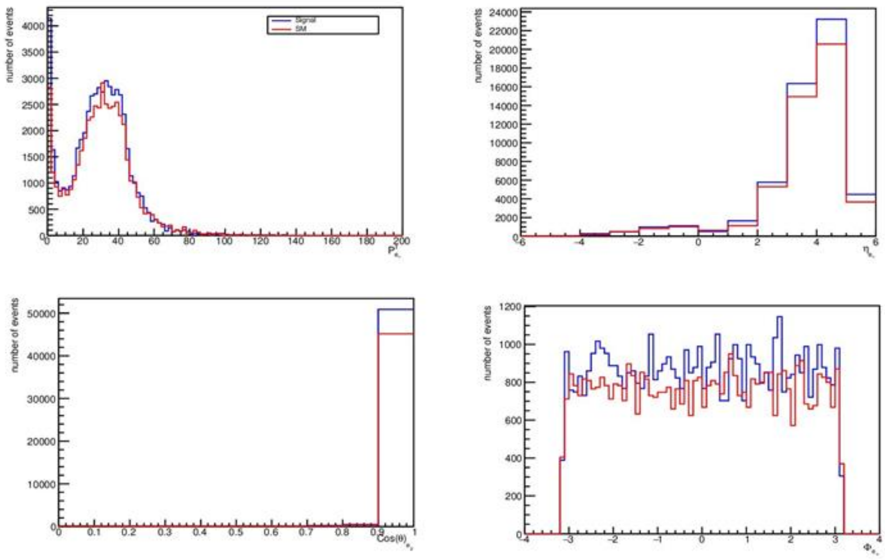

Figure 4.20. The distributions of the for transverse momentum of sub leading electron $P_{e_2}^T$(top left), pseudo-rapidity η_{e_2}(top right), cosθ_{e_2}(bottom left) and the azimuthal angle ϕ_{e_2}(bottom right) for the process e p → ν_e Z q → ν_e e^+ e^- q at the FCC-he collider for a chosen values κ_{ut} = κ_{ct}= 0.1.

In Figure 4.21, we plot the kinematic distributions of the quark in the process e p → υ_e Z q → υ_e e^+e^-q namely, the transverse momentum $P_{q_1}^T$ (top left), pseudo-rapidity η_{q_1} (top right), cos θ_{q_1} (bottom left) and the azimuthal angle ϕ_{q_1} (bottom right). We conclude from these distributions that the behavior of the signal and the SM is close to each other.

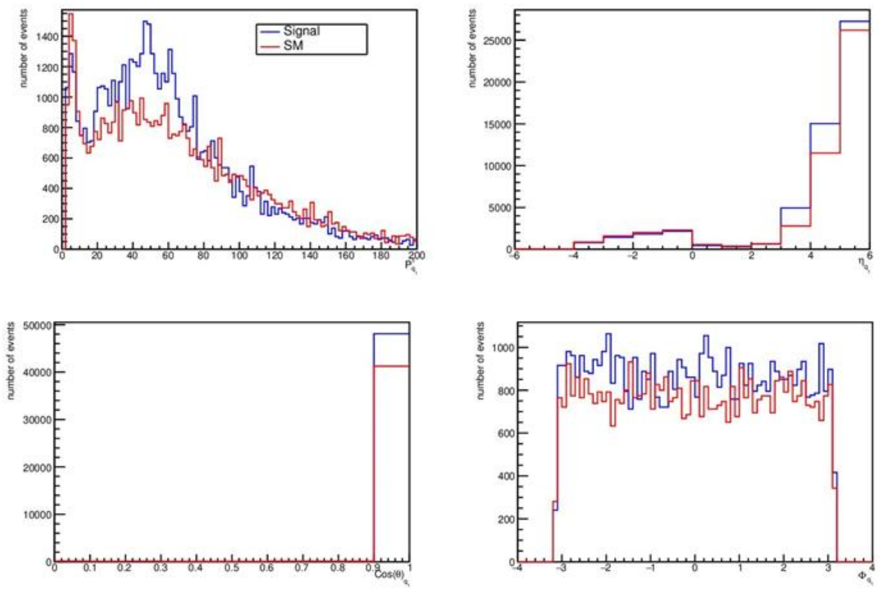

Figure 4.21. The distributions of the transverse momentum P_{q1}^{T} (top left), pseudo-rapidity η_{q_1}(top right), cos θ_{q_1}(bottom left) and the azimuthal angle ϕ_{q_1}(bottom right) of the quark corresponding to the process e p → ν_e Z q → ν_e e^+ e^- q at the FCC-he collider for a chosen values $\kappa_{ut} = \kappa_{ct} = 0.1$.

In Figure 4.22, we present our results of the distributions of the angular separation between final state particles e_1, e_2 and q_1, ΔR_{e1e2} (top left), $\Delta R_{e_1 q_1}$(top right), $\Delta R_{e_2 q_1}$ (bottom left), and the missing transverse energy MET (bottom right).

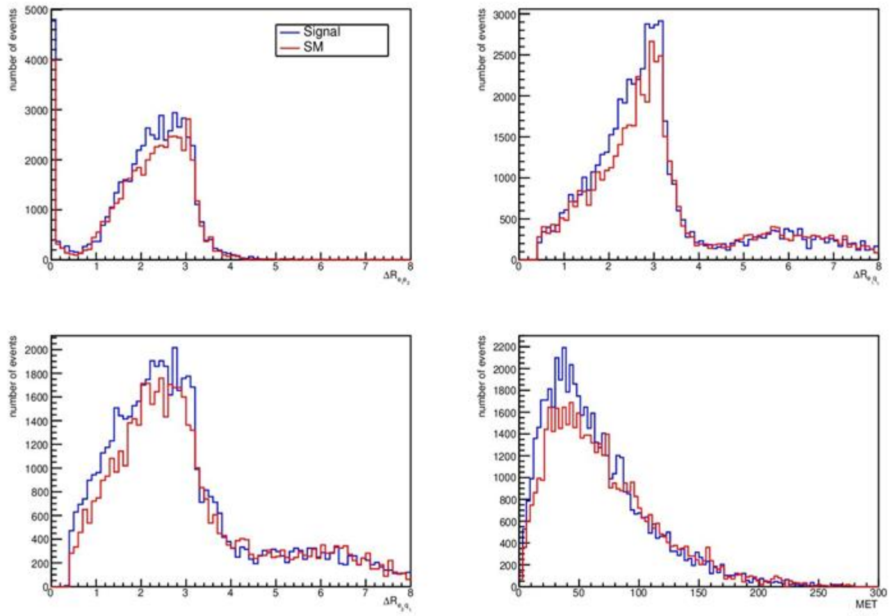

Figure 4.22. The distributions of the angular separations $\Delta R_{e_1 e_2}$ (top left), $\Delta R_{e_1 q_1}$(top right), $\Delta R_{e_2 q_1}$(bottom left), as well as MET (bottom right) for the process e p → ν_e Z q → ν_e e^+ e^- q at the FCC-he collider for a chosen values κ_{ut} = κ_{ct} = 0.1.

In Figure 4.23, we show the kinematic distributions of both signal and SM of the invariant mass of the Z boson of two electrons M_{e1e2} (left) and the invariant mass M_{e1e2q1}(right) where the reconstructed mass of two electrons is demanded to lay between 86 GeV < $M_{e_1 e_2}$< 92 GeV. From the right plot in the figure, we see the peak of the signal is shifted around invariant mass $M_{e_1 e_2 q_1} = 170$ GeV approximately and becomes larger than the SM background compared with the left plot.

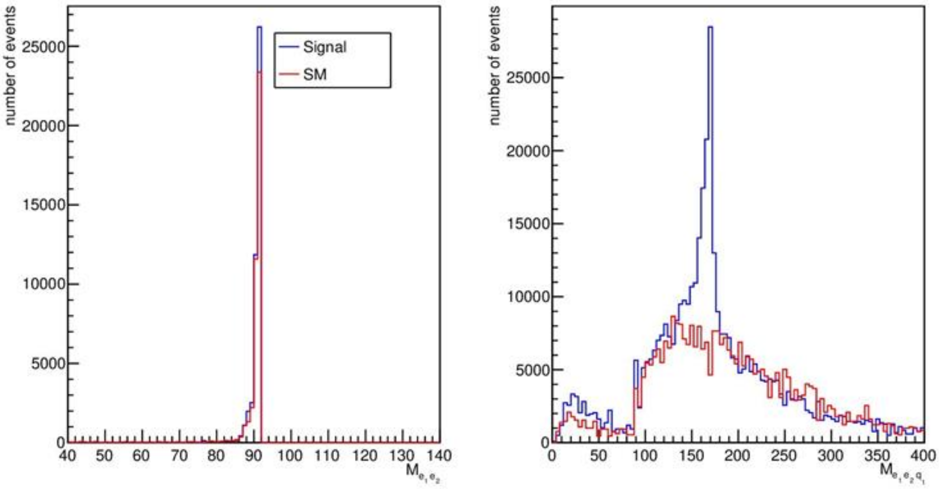

Figure 4.23. Invariant mass distributions of the Z boson for two electrons $M_{e_1e_2}$ (left) while the right plot includes invariant mass for Z boson with one quark $M_{e_1e_2q_1}$ at FCC-he collider.

4.4.2 e p → ν_e Z q → ν_e $\mu^+\mu^-$ q

In the following figures, we show our plots for the e p → υ_e Z q → υ_e $\mu^+ \mu^- q$ process at the FCC-he future collider with integrated luminosity 1 ab^{-1}. To assess the kinematic distributions of the final state particles for both the signal and SM background in this channel, we use the coupling values κ_{ut}=κ_{ct} = 0.3.

Figure 4.24, elucidates the kinematic distributions for both SM background and signal. We conduct the same analysis as we did for the case of e p → υ_e Z q → υ_e $e^+ e^- q$. The distributions in the figure are shown for the transverse momentum of leading muon $P^T_{\mu 1}$ (top left), pseudo-rapidity η_{μ_1}(top right), cos θ_{μ_1} (bottom left), and azimuthal angle ϕ_{μ_1} (bottom right) corresponding to the process e p → υ_e Z q → υ_e $\mu^+ \mu^- q$. The plots in the figure show that, enhancements correspond to the value of the transverse momentum and pseudo-rapidity laying in the range [40 GeV- 80 GeV] and [3,4] respectively.

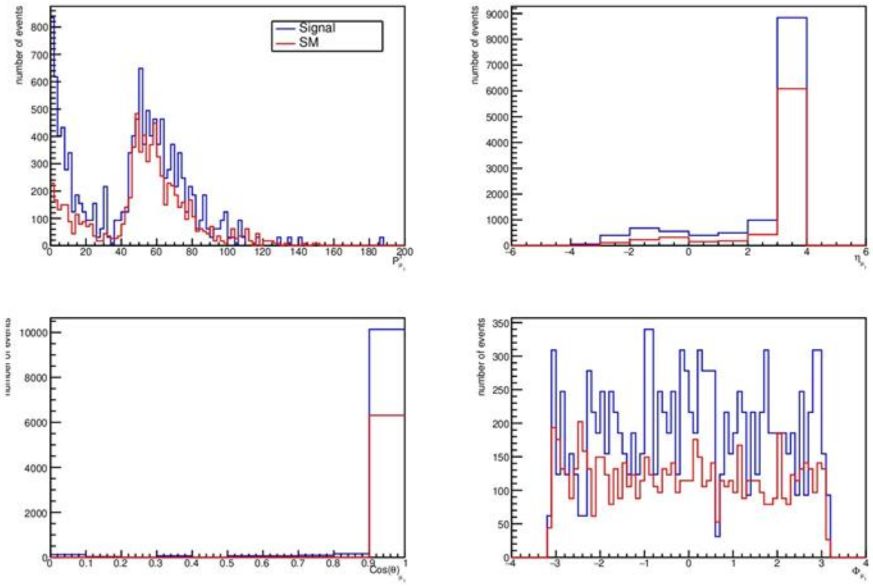

Figure 4.24. The distributions of the transverse momentum of the leading muon $P^T_{\mu 1}$ (top left), pseudo-rapidity η_{μ_1} (top right), cos θ_{μ_1} (bottom left) and the azimuthal angle ϕ_{μ_1} (bottom right) corresponding to the process e p → ν_e Z q → ν_e $\mu^+ \mu^-$ q at the FCC-he collider for a chosen values $\kappa_{ut} = \kappa_{ct} = 0.3$.

The kinematic distributions for the subleading muon and for the same process are presented in Figure 2.25, the transverse momentum sub leading muon $P^T_{\mu 2}$ (top left), pseudo-rapidity η_{μ_2}(top right), cosθ_{μ_2}(bottom left), and azimuthal angle ϕ_{μ_2} (bottom right). Given this, the plots in the Figure 2.25 demonstrate that the transverse momentum has a low impact on enhancing the signal and approximately the same for pseudo-rapidity and cos θ_{μ_2} however, the large effect for the enhancements is due to the azimuthal angle ϕ_{μ_2}.

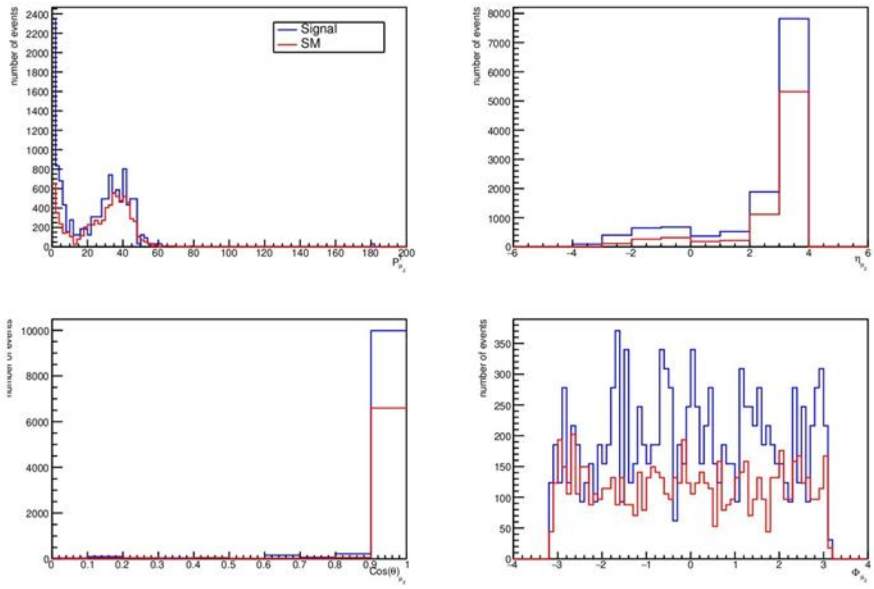

Figure 4.25. The distributions of the transverse momentum of the sub leading muon $P_{\mu 2}^{T}$ (top left), pseudo-rapidity η_{μ_2} (top right), cos θ_{μ_2} (bottom left) and the azimuthal angle ϕ_{μ_2}(bottom right), corresponding to the process e p → ν_e Z q → ν_e $\mu^+\mu^-$ q at the FCC-he collider for a chosen values $\kappa_{ut} = \kappa_{ct} = 0.3$.

The kinematic distributions of the quark in the decay channel e p → υ_e Z q → υ_e μ^+ μ^-q are presented in Figure 4.26, including transverse momentum P_{q1}^{T} (left plot), pseudo-rapidity, cos θ_{q_1} (right plot) and the azimuthal angle ϕ_{q_1}(bottom right). From the distributions in the figure the enhancements of the signal compared to the SM background occur at values of the transverse momentum, and pseudo-rapidity, lay in the ranges [30 GeV, 60GeV], [4, 6], respectively.

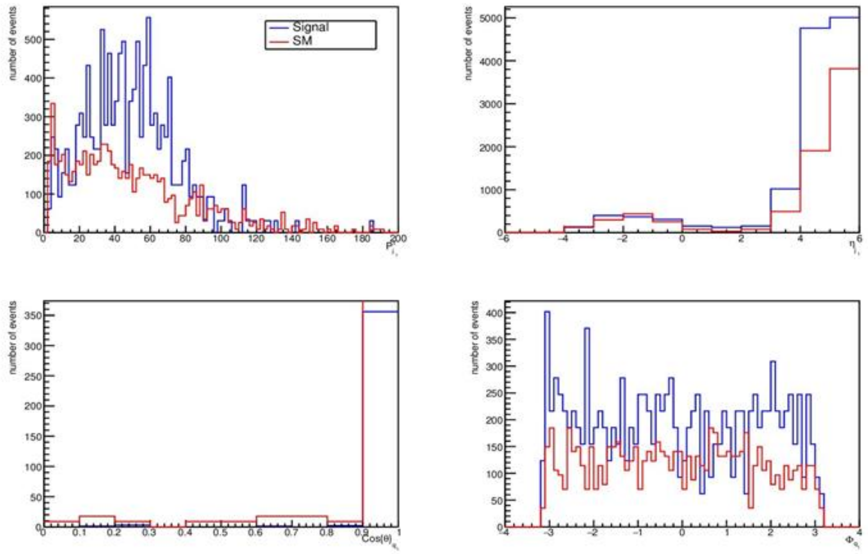

Figure 4.26. The distributions of the transverse momentum $P^T_{q_1}$ (top left), pseudo-rapidity η_{q_1} (top right), cos θ_{q_1} (bottom left) and the azimuthal angle ϕ_{q_1} (bottom right) of the quark at the FCC-he collider for a chosen values $\kappa_{ut} = \kappa_{ct}$= 0.3.

Figure 4.27, shows the distributions of the angular the distances between finale state μ_1, μ_2 and $q_{1,}$ where $\Delta R_{\mu_1,\mu_2}$ (top left), $\Delta R_{q_1\mu_1}$ (top right), $\Delta R_{q_1\mu_2}$ (bottom left) as well as the Missing Transverse Energy MET (bottom right).

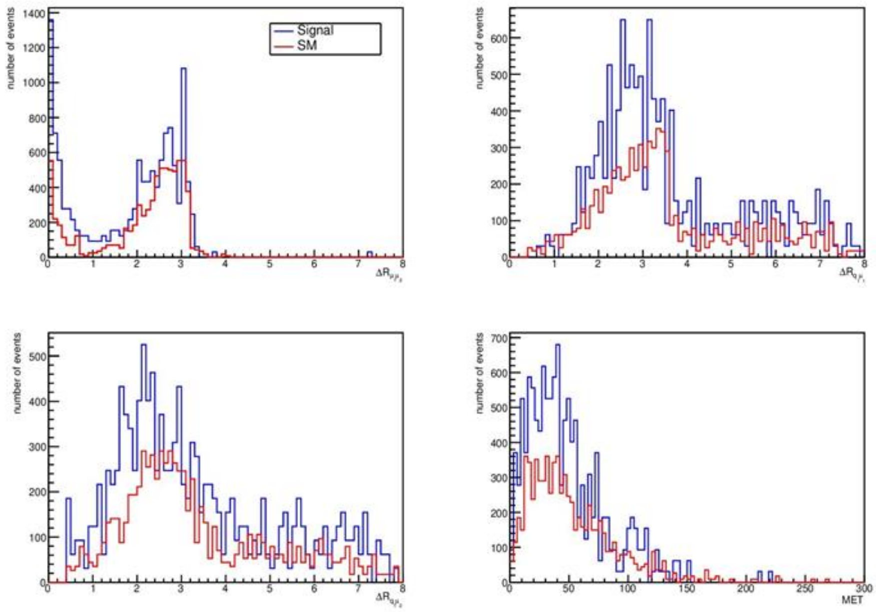

Figure 4.27. The distributions of the angular separation: top left $\Delta R_{\mu_1,\mu_2}$, top right $\Delta R_{q_1\mu_1}$ bottom left $\Delta R_{q_1\mu_2}$ as well as MET (bottom right) at FCC-he collider.

Figure 4.28, depicts the kinematic distributions of both signal and SM of the invariant mass of the Z boson reconstructed from leadind and subleading muon $M_{\mu_1\mu_2}$ (left) and the invariant mass of two muons with one quark $M_{\mu_1\mu_2q_1}$ (right). The reconstructed mass of two muons must be in the range 86 GeV < $M_{\mu_1\mu_2}$ < 92 GeV. It is obvious from the right plot that the signal is remarkably increased compared with the SM background and has a peak in the left plot at roughly a value of $M_{\mu_1\mu_2q_1} = 170$ GeV.

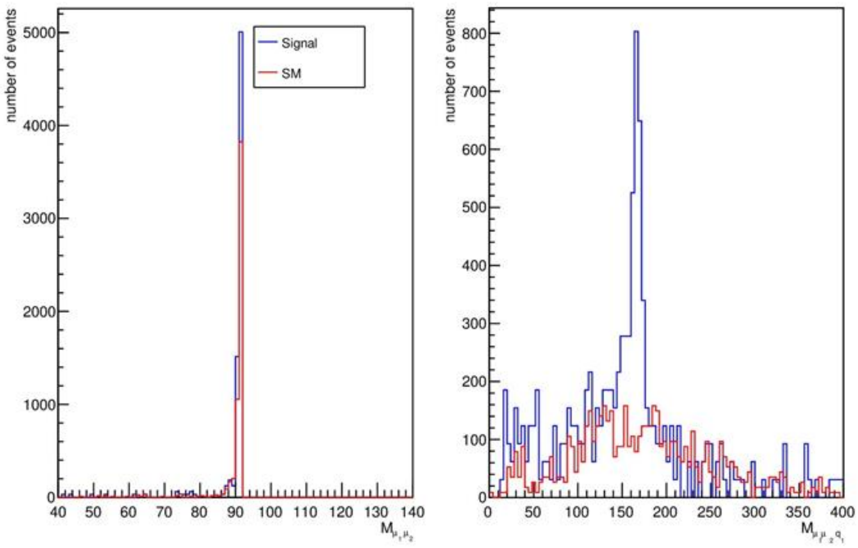

Figure 4.28. Invariant mass distributions of Z boson $M_{\mu_1\mu_2}$ (left-handed) while the (right-handed) includes the invariant mass for Z boson and one quark $M_{\mu_1\mu_2q_1}$for the signal and background at FCC-he.

4.4.3 e p → ν_e Z q → ν_e q $\bar{q}$ q

In the following figures, the results are offered for the FCC-he future collider with integrated luminosity 1 ab^{-1}. To obtain the kinematic distributions of the final state particles for both the signal and the SM background, we use the coupling values at $\kappa_{ut} = \kappa_{ct}$ = 0.1. Here, we take into account the two jets produced by the decay of the Z boson.

Figure 4.29, shows the kinematic distributions the transverse momentum of the leading jet $P_{j_1}^T$ (top left), pseudo-rapidity η_{j_1} (top right), cos θ_{j_1}(bottom left) and the azimuthal angle ϕ_{j_1}(bottom right) corresponding to the process e p → υ_e Z q → υ_e $q\bar{q}\,q$. We see from the figure that the enhancements happen for transverse momentum varies within the range [25 GeV,90 GeV], the pseudo-rapidity values roughly in the range [4,6] respectively.

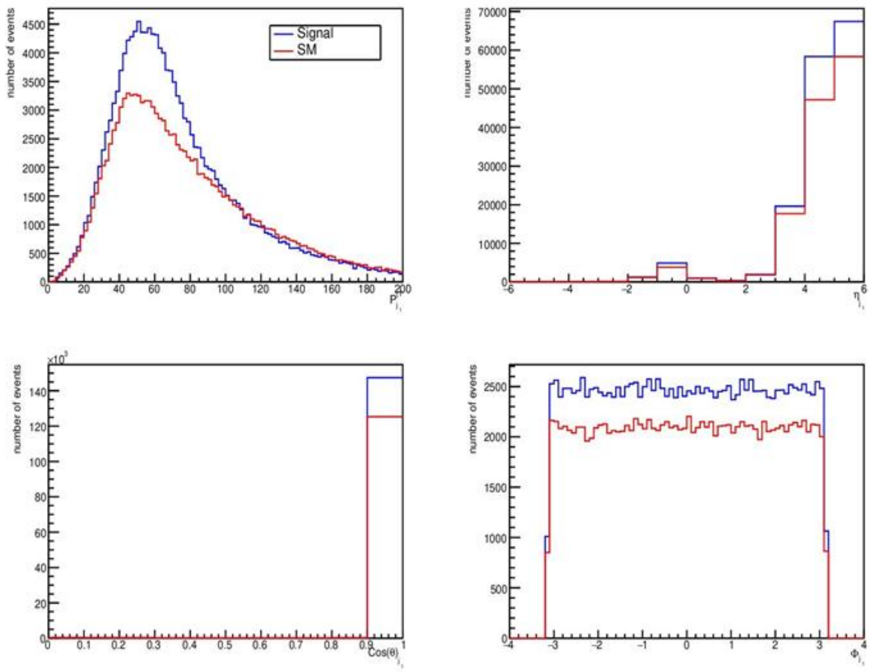

Figure 4.29. The distributions of the transverse momentum of the leading jet $P^T_{j_1}$ (top left), pseudo-rapidity η_{j_1} (top right), $\cos\theta_{j_1}$ (bottom left) and the azimuthal angle ϕ_{j_1} (bottom right), at FCC-he collider for a chosen values $\kappa_{ut} = \kappa_{ct} = 0.1$.

We display the distributions for the transverse momentum of the sub leading jet $P^T_{j_2}$, pseudo-rapidity η_{j_2}, $\cos\theta_{j_2}$, and azimuthal angle ϕ_{j_2} in Figure 4.30. We conclude from the plots that the increments in the signal associated with transverse momentum between [20 GeV - 60 GeV], pseudo-rapidity values roughly in the range [4,6], and values of $\cos\theta_{j_2}$ close to one.

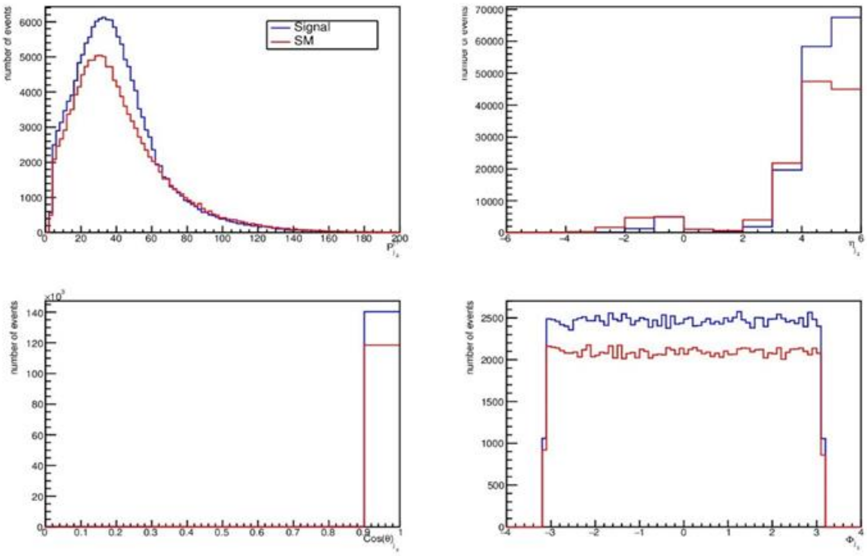

Figure 4.30. The distributions of the transverse momentum of the subleading jet $P_{j_2}^T$ (top left), pseudo-rapidity η_{j_2}(top right), cosθ_{j_2}(bottom left) and the azimuthal angle ϕ_{j_2} (bottom right) at FCC-he collider for a chosen values $\kappa_{ut} = \kappa_{ct}$= 0.1.

Now we look at the kinematic distributions of the quark produced by the process $e\,p \rightarrow \upsilon_e\, Z\; q \rightarrow \upsilon_e\; q\,\overline{q}\,q$ at FCC-he collider. The related kinematic distributions are shown in Figure 4.31. From the plots in the figure we note that large enhancements can not be obtained in this case.

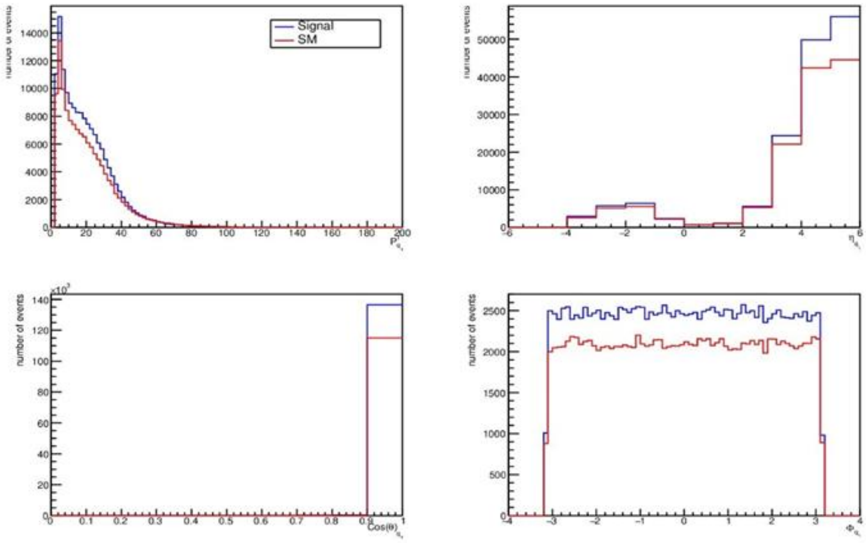

Figure 4.31. The distributions of the transverse momentum P_{q1}^{T} (top left), pseudo-rapidity η_{q_1}(top right), cosθ_{q_1}(bottom left) and the azimuthal angle ϕ_{q_1} (bottom right) of the quark. corresponding to the process $e\,p \rightarrow \upsilon_e\, Z\, q \rightarrow \upsilon_e\ \ q\,\overline{q}\,q$ at FCC-he collider for a chosen values $\kappa_{ut} = \kappa_{ct}$ =0.1.

The distributions of the angular distances of the leading for jet $\Delta R_{j_1 j_2}$ (top left), leading jet with one quark $\Delta R_{j_1 q_1}$(top right), and subleading jet with one quark $\Delta R_{j_2 q_1}$ (bottom left), as well as missing transverse energy MET (bottom right) are demonstrated in Figure 4.32.

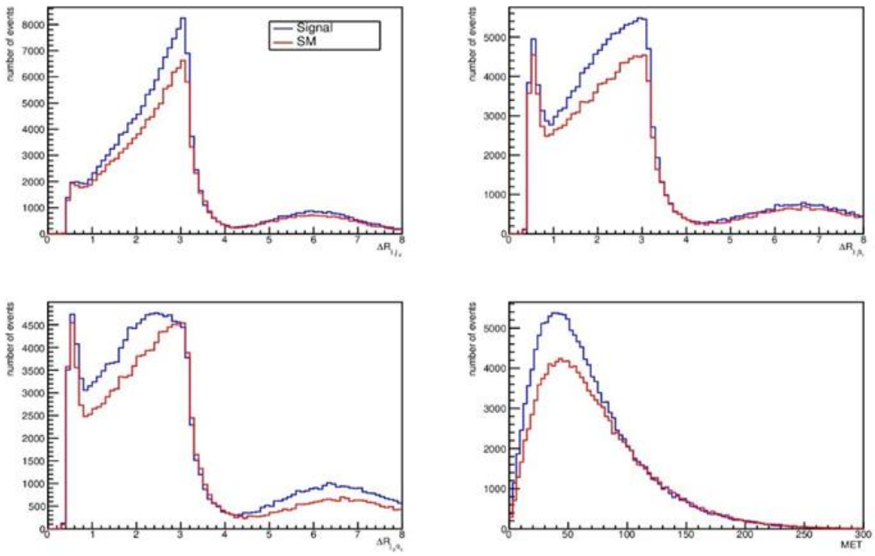

Figure 4.32. The angular separation top left $\Delta R_{j_1 j_2}$, top right $\Delta R_{j_1 q_1}$, bottom left $\Delta R_{j_2 q_1}$, as well as MET (bottom right) at FCC-he collider using the coupling $\kappa_{ut} = \kappa_{ct}$ = 0.1.

Figure 4.33, shows the distributions of the invariant masses of the Z boson reconstructed from the two jets M_{j1j2} and M_{j1j2q1} for both the signal and the SM. We require that the reconstructed masses of the two jets be in the 86 GeV$<$ $M_{j_1j_2} <$ 92 range (left plot).

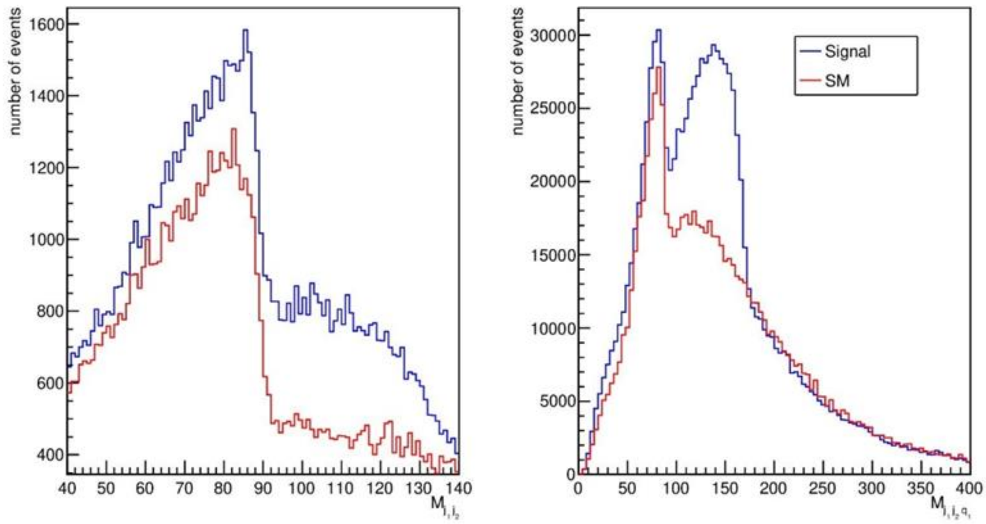

Figure 4.33. Invariant mass distributions of Z boson (left-handed) of two jets $M_{j_1j_2}$ while the (right-handed) $M_{j_1j_2q_1}$ at FCC-he using the coupling $\kappa_{ut} = \kappa_{ct} =$ 0.1.

In Table 4.1, we display the kinematic cuts utilized in our analysis of the signal and the background at LHeC and FCC-he colliders with L_{int} = 1 ab^{-1}. In order to select signal events, we demand having two oppositely charged light leptons and one jet in the final state. Particles are ordered according to the highest transverse momentum. Regarding the invariant mass of the two oppositely charged light leptons and the two jets obtained from the Z decay, we require their invariant mass to be close to the Z boson mass. The selected values of the other cuts are chosen to improve the signal in comparison with the background, as is shown in the figures below for all decay channels.

Table 4.1. Events selection and kinematic cuts are utilized for the analysis of signal and background at LHeC and FCC-he colliders with L_{int} = 1 ab^{-1}.

Accelerator	Decay channels	Cuts
LHeC	e^+e^-	Pe_1^T> 30 GeV, P_{e2}^T> 20 GeV, P_{q1}^T> 30 GeV and 2 < η (e_1,e_2 ,q_1) < 6 invariant mass 86 GeV < $M_{e_1e_2}$< 92 GeV $\Delta R_{e_1e_2}$> 0.7, $\Delta R_{e_1q_1}$> 0.7, $\Delta R_{e_2q_1}$> 0.7 and MET >10 GeV
	$\mu^+\mu^-$	$P_{\mu1}^T$> 30 GeV, $P_{\mu2}^T$ > 20 GeV, P_{q1}^T> 30 GeVand 2 < η (μ_1, μ_2, q_1) <6 invariant mass 86 GeV< $M_{\mu1\mu2}$ < 92 GeV $\Delta R_{\mu_1\mu_2}$> 0.7, $\Delta R_{\mu_1q_1}$ > 0.7, $\Delta R_{\mu_2q_1}$> 0.7 and MET >10 GeV
	$q\bar{q}$	P_{j1}^T >30 GeV, P_{j2}^T> 20 GeV, P_{q1}^T> 30 GeV and 2 < η (j_1, j_2, q_1) < 6 invariant mass 86 GeV < $M_{j_1j_2}$< 92 GeV $\Delta R_{j_1j_2}$> 0.7, $\Delta R_{j_1q_1}$ > 0.7, $\Delta R_{j_2q_1}$ > 0.7 and MET >10 GeV
FCC-he	e^+e^-	Pe_1^T> 20 GeV, P_{e2}^T> 25 GeV, P_{q1}^T> 15 GeV and 2 < η (e_1,e_2 ,q_1) < 6 invariant mass 86 GeV< $M_{e_1e_2}$< 92 GeV $\Delta R_{e_1e_2}$> 0.7, $\Delta R_{e_1q_1}$ > 0.7, $\Delta R_{e_2q_1}$> 0.7 and MET >10 GeV
	$\mu^+\mu^-$	$P_{\mu1}^T$> 40 GeV, $P_{\mu2}^T$20 GeV, P_{q1}^T> 25 GeV and 2 < η (μ_1, μ_2, q_1) < 6 invariant mass 86 GeV < $M_{\mu1\mu2}$< 92 GeV $\Delta R_{\mu_1\mu_2}$> 0.7, $\Delta R_{\mu_1q_1}$> 0.7, $\Delta R_{\mu_2q_1}$ > 0.7 and MET >10 GeV
	$q\bar{q}$	P_{j1}^T >30 GeV, P_{j2}^T> 20 GeV , P_{q1}^T> 30 GeV and 2 < η (j_1, j_2, q_1) < 6 invariant mass 86 GeV < $M_{j_1j_2}$< 92 GeV $\Delta R_{j_1j_2}$> 0.7, $\Delta R_{j_1q_1}$ > 0.7, $\Delta R_{j_2q_1}$> 0.7 and MET >10 GeV

Figures 4.34 and 4.35, demonstrate the distribution of the invariant mass M_{Zq} for different decay channels of Z boson without (left) and with (right) the cuts for the LHeC and FCC-he colliders respectively. The Z boson is reconstructed from e^+e^-, $\mu^+\mu^-$and $q\bar{q}$ are shown in the top, middle and bottom rows, respectively. From all these figures we can see the effect of optimized cuts used in the analysis. Applying these cuts allows us to see the impacts of the cuts on the signal and the background. The aim is to obtain the cuts that optimize the discrimination between signal and background and eventually allows us to evaluate the statistical significance.

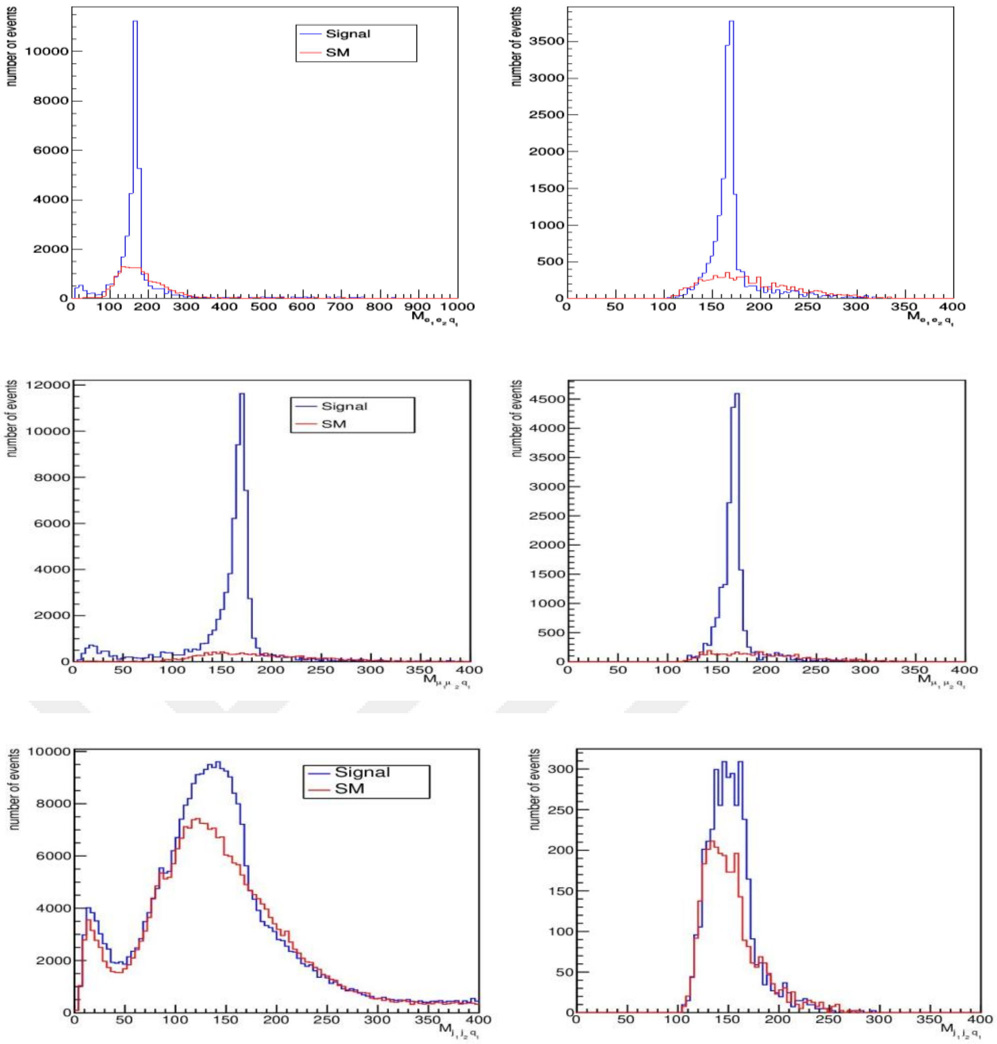

Figure 4.34. Distributions of invariant mass M_{zq} for different decay channel of Z boson (e^+e^-, $\mu^+\mu^-$ and $q\bar{q}$) with and without optimized cuts (right column and left column , respectively) for LHeC.

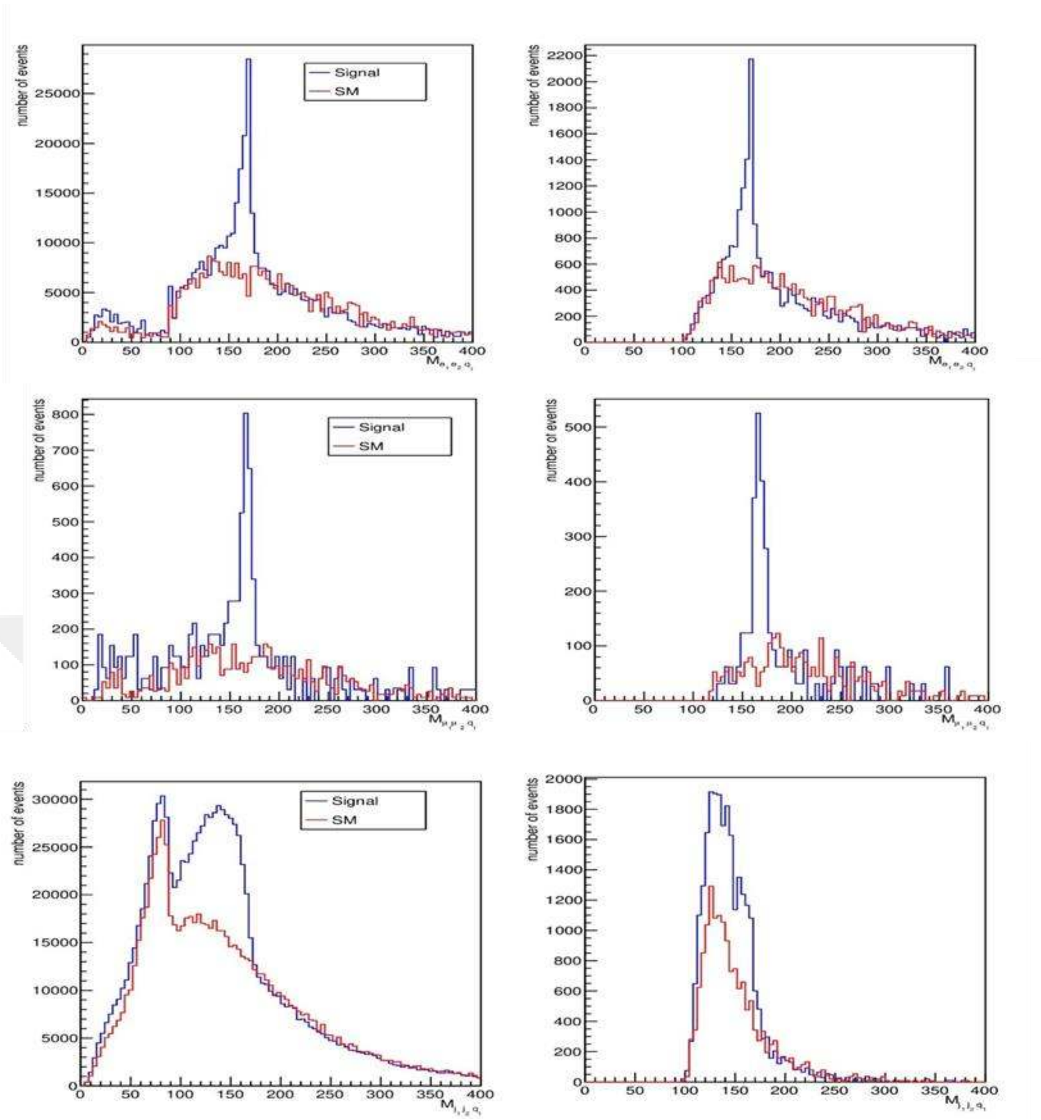

Figure 4.35 . Distributions of invariant mass M_{zq} for different decay channel of Z boson (e^+e^-, $\mu^+\mu^-$ and $q\bar{q}$) with and without optimized cuts (right column and left column, respectively) for FCC-he.

4.5 The statistical significance

Statistical significance is the notion that a set of observed data is not random but can instead be arising from a certain reason. In other words, it lends credibility to the notion that the results are real and not caused by luck or chance.

In this section, we evaluate the statistical significance (SS) of the process $e\,p \rightarrow \upsilon_e\,Z\,q$ at LHeC and FCC-he future colliders with integrated luminosity 1 ab^{-1}. The distributions of the reconstructed Z bosons with one quark M_{Zq}, given in figure 4.34 for the LHeC collider and figure 4.35 for the FCC-he collider, for all decay channels are normalized to the integrated luminosity 1 ab^{-1} and the range between 140 GeV $< M_{Zq} <$ 180 GeV, is utilized to compute Statistical Significance (32) which is defined as

$$SS = \sqrt{2[(S+B)In(1+\frac{S}{B}) - S\,]}$$

In order to quantify the SS, we evaluate S+B (blue curve) and the total background (B) (red curve), then we estimate the signal (S) by taking the difference between S+B and B events at a given specific integrated luminosity after applying the final cuts. The results of the SS rely on the considered values of the couplings $\kappa_{ut} = \kappa_{ct}$ at $L_{int} = 1ab^{-1}$ and on the final states originating from the Z decays namely, the leptonic (electron and muon) ones and the hadronic ones. Consequently, with the help of the evaluated SS, we can fit the significance as a function of the couplings. Moreover, this fit can be used to impose upper limits on these couplings and hence these limits can be adopted to calculate the branching ratios for the given process for each collider considered in this study.

In Table 4.2, we provide our results of the statistical significance for the leptonic final states channels corresponding to a selected set of values of the effective couplings $K_{ut} = K_{ct}$ at the LHeC and FCC-he colliders. We see from the Table 4.2, in both colliders, the SS increases with increasing the value of the effective couplings. We remark also from the table that, large couplings lead to remarkably large values of the SS

Table 4.2. The estimated SS for selected values of the couplings for leptonic final states channels at LHeC and FCC-he colliders.

LHeC		FCC-he	
Couplings	SS	Couplings	SS
0.05	11.9937	0.008	0.744842
0.07	14.19	0.01	5.75491
0.1	32.7633	0.05	15.8986
0.3	171.616	0.07	32.1202
0.5	341.072	0.1	59.2944
0.7	524.24	0.3	295.574

Figure 4.36, illustrates the statistical significance (SS) of the $e\,p \rightarrow \upsilon_e\, Z\, q$ process as a function of the couplings for the leptonic final state channels (electron and muon) at L_{int}=1 ab^{-1} for LHeC (left plot) and for FCC-he (right plot). As can be seen from the left plot in the figure, the upper limit of the coupling reaches the value 0.024 at 3σ SS (see the black line in the plot) for the LHeC collider while for the FCC-he collider the upper limit of the coupling approaches the value equal to 0.0172 at 3σ SS as indicated from the black line in the right plot. It should be noted that we used the fit function of $K = ax^3 + bx^2 + cx$ and represented by the red line in the figure. The values of SS versus the couplings are listed briefly in table 4.2 for LHeC and FCC-he future colliders.

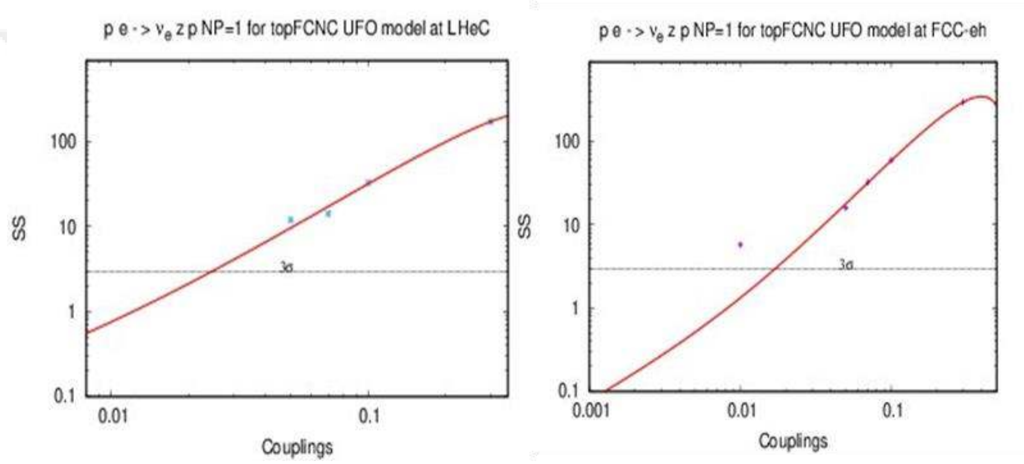

Figure 4.36. Statistical significance as a function of the anomalous FCNC couplings after applying the cuts of finale state for leptonic channels at $L_{in\,t}$=1 ab^{-1} for LHeC (left) and the FCC-he (right).

In Table 4.3, we show our obtained results of the statistical significance for the hadronic final states channels for a set of values of the effective couplings K_{ut}= K_{ct} at the LHeC and FCC-he colliders. We note from Table 4.3 that, the SS increases with increasing the value of the effective couplings for both colliders. Moreover, one can notice from the table that, large couplings yield considerably large values of the SS.

Table 4.3. The evaluated SS for a set of selected values of the couplings for hadronic final states channels at LHeC and FCC-he colliders.

LHeC		FCC-he	
Couplings	SS	Couplings	SS
0.05	2.22178	0.008	1.7226
0.07	7.88512	0.03	3.0772
0.1	23.0855	0.05	16.9153
0.3	105.757	0.07	36.6093
0.5	219.882	0.1	63.0251
0.7	335.979	0.3	331.917

In Figure 4.37, we display the statistical significance (SS) of the process $e\, p \rightarrow \upsilon_e\, Z\, q$ as function of the couplings for the hadronic final states channels at L_{int}=1 ab^{-1} for LHeC collider (left plot) and FCC-he collider (right plot). As in Figure 4.37 the black color represents the 3σ SS and the red line represents the fit function $K = ax^3 + bx^2 + cx$. Plainly from the Figure 4.37 , the upper limits of the couplings are 0.03 and 0.0216 for LHeC and FCC-he colliders, respectively.

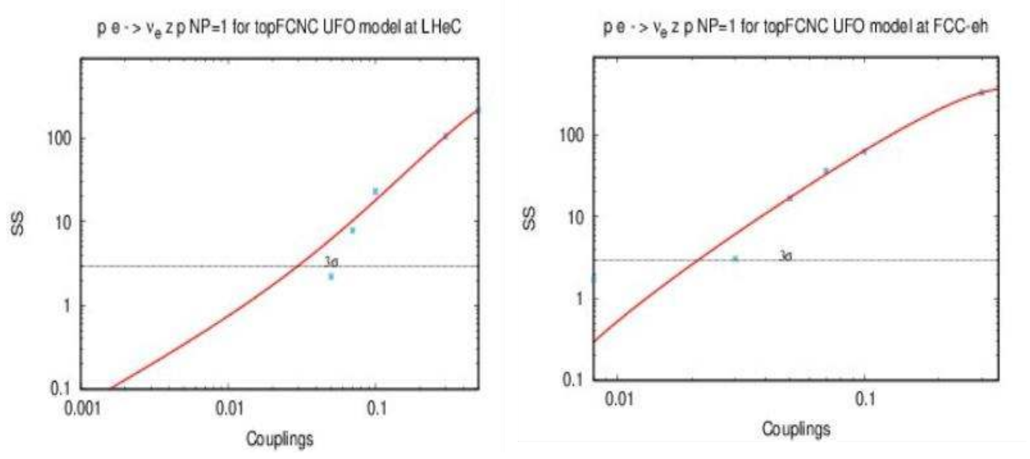

Figure 4.37. Statistical significance as a function of the anomalous FCNC couplings after applying the cuts for hadronic channels L_{int}=1 ab^{-1} for LHeC (left) and the FCC-he (right).

5. CONCLUSIONS

Searching for the top quark FCNC in the vertex tZq, where q points out u or c quark at electron-proton colliders can be a good probe for NP beyond the Standard Model. Particularly, due to the absence of such FCNC vertex in the SM at the tree-level.

In this thesis, we have examined the $ep \rightarrow \upsilon_e\, Z\, q$ process followed by Z boson decaying into two leptons or two jets at the future electron hadron colliders under consideration, LHeC and FCC-he with an integrated luminosity 1 ab^{-1}. We have generated the signal and background events for the $e\, p \rightarrow \upsilon_e\, Z\, q$ process using MadGraph5_aMC@NLO, and Delphes was utilized for realistic detector effects. We have evaluated the cross sections of the $e\, p \rightarrow \upsilon_e\, Z\, q$ process for different scenarios of the parameter κ_q contributing to the signal. We have found that non-vanishing κ_{ut} and κ_{ct} can enhance the cross section.

We also executed an analysis of the kinematic distributions including the transverse momentum, pseudo-rapidity and invariant mass distribution of the Z boson. In addition, we have applied a cut on the invariant mass of the final state to evaluate the statistical significance. Our goal for doing this is to obtain the best limits on the anomalous top FCNC tqZ couplings and give an estimation of the upper values of the branching ratios of the given final states. The computation of the branching ratio of the decay mode t→qZ has been found using Eq (1.8). We find the branching ratios BR $(t \rightarrow qZ) = 8 \times 10^{-4}$ (4×10^{-4}) for the channel $Z \rightarrow \ell^+\ell^-$ while BR $(t \rightarrow qZ) = 1.2 \times 10^{-3}$ (6×10^{-4}) for the channel $Z \rightarrow q\bar{q}$ at LHeC (FCC-he) collider. We deduce from these results that FCC-he has the best limits for the leptonic channel.

We compare our results for $ep \rightarrow \upsilon_e\, Z\, q$ process for BR (t →qZ) with its prediction in the SM and other colliders given in the literature. Within SM, has found BR $(t \rightarrow cZ) \sim 10^{-14}$(55). Furthermore, at the LHC the CMS collaboration utilizing a combined result for the tqZ couplings (via anomalous tZ production) has enhanced the limits BR $(t \rightarrow uZ) \leq 2.2 \times 10^{-4}$ and BR $(t \rightarrow cZ) \leq 4.9 \times 10^{-4}$ (56). Considering the High Luminosity Large Hadron Collider (HL-LHC) with $L_{int} = 3$ ab^{-1} the limits on the top FCNC were estimated to be BR $(t \rightarrow uZ) \leq 4.3 \times 10^{-5}$and

BR (t →cZ) ≤ 5.8 × 10^{-5} (57) at 95% C.L. Regarding other future colliders, the sensitivities to the top quark FCNC interactions have been assessed on the BR (t → uZ) ≤ 10^{-5} for the HL-LHC with √s = 14 TeV and L_{int} = 3 ab^{-1}. A recent study carried out in Ref (58) about the search for Zt production at FCC-hh with √s = 100 TeV and Lint = 10 ab^{-1} found that the BR (t → uZ) ≤ 10^{-6} and BR (t → cZ) ≤ 10^{-5}. In Ref (32) limits for the branching BR(t → qZ) for 1 ab^{-1} luminosity projections at LHeC and FCC-he were estimated to be BR (t → qZ) ≤ 4.0 × 10^{-5} and BR (t → qZ) ≤ 9.5 × 10^{-6} respectively for the e^-p → e^- Wq +X processs.

Comparing our results with the obtained results above in other colliders, we find that at LHeC and FCC-eh colliders the obtained limits on the branching ratio via the e p → υ_e Z q process is comparable. One can improve these results with new machine learning techniques such as Boosted Decision Tree (BDT).

6. REFERENCES

"Vancouver citation system was used in this thesis"

(1-58)

1. Zhang W. Top Quark Studies with the CMS Experiment: Rare Process and Precision Measurements. Brown University (US); 2022.

2. Peskin ME. Beyond the standard model. arXiv Prepr hep-ph/9705479. 1997.

3. Cottingham WN, Greenwood DA. An introduction to the standard model of particle physics. Cambridge university press; 2007.

4. Griffiths D. Introduction to elementary particles. John Wiley & Sons; 2020.

5. F. Halzen and AD Martin: Quarks and Leptons, John Wiley and Sons, New York, 1984, 396 , 9,580 . 1984;39(11):864.

6. Protopapadaki ES. ZZ diboson measurements with the ATLAS detector at the LHC and study of the toroidal magnetic field sensors. Saclay; 2014.

7. Gounaris GJ, Layssac J, Renard FM. New and standard physics contributions to anomalous Z and γ self-couplings. Phys Rev D. 2000;62(7):73013.

8. Fritzsch H, Gell-Mann M, Leutwyler H. Advantages of the Color Octet Gluon Picture. In: Murray Gell-Mann: Selected Papers. World Scientific; 2010. p. 262–5.

9. Hanzel F, Martin AD. Quarks and Leptons: An introductory course in modern particle phyics. John Wiley & Sons; 1984.

10. Electroweak TSLD, Groups HF, Collaboration A, Collaboration D, Collaboration L, Collaboration O, et al. Precision electroweak measurements on the Z resonance. Phys Rep. 2006;427(5–6):257–454.

11. CMS Collaboration cms-publication-committee-chair@ cern. ch. A portrait of the Higgs boson by the CMS experiment ten years after the discovery. Nature. 2022 Jul 7;607(7917):60-8.

12. Gell-Mann M, Lévy M. The axial vector current in beta decay. Nuovo Cim. 1960;16(4):705–26.

13. Abe F, Akimoto H, Akopian A, Albrow MG, Amendolia SR, Amidei D, et al. Observation of top quark production in p p collisions with the Collider Detector at Fermilab. Phys Rev Lett. 1995;74(14):2626.

14. Abachi S, Abbott B, Abolins M, Acharya BS, Adam I, Adams DL, et al. Direct measurement of the top quark mass. Phys Rev Lett. 1997;79(7):1197.

15. Abachi S, Abbott B, Abolins M, Acharya BS, Adam I, Adams DL, Adams M, Ahn S, Aihara H, Alitti J, Alvarez G. Observation of the top quark. Physical review letters. 1995 Apr 3;74(14):2632.

16. Bernreuther W, Si Z-G. Top quark and leptonic charge asymmetries for the Tevatron and LHC. Phys Rev D. 2012;86(3):34026.

17. Abazov VM, Abbott B, Abolins M, Acharya BS, Adams M, Adams T, Agelou M, Ahn SH, Ahsan M, Alexeev GD, Alkhazov G. Experimental discrimination between charge 2 e/3 top quark and charge 4 e/3 exotic quark production scenarios. Physical review letters. 2007 Jan 22;98(4):041801.

18. ATLAS C, Agustoni M, Ancu L, Battaglia A, Beck HP, Borer C, et al. Measurement of the top quark charge in pp collisions at sqrts= 7 TeV with the ATLAS detector. J High Energy Phys. 2013;1311(11):31.

19. Khachatryan V, Sirunyan AM, Tumasyan A, Adam W, Asilar E, Bergauer T, et al.

Measurement of the top quark mass using proton-proton data at (s)= 7 and 8 TeV. Phys Rev D. 2016;93(7):72004.

20. collaboration A. Measurement of the top quark mass in the $ t\bar {t}\to $ lepton+ jets channel from $\sqrt {s}= 8$ TeV ATLAS data and combination with previous results. arXiv Prepr arXiv181001772. 2018;

21. Poggi R. Top-quark pair production cross-section measurements in the all-hadronic decay channel at the ATLAS experiment and hardware-based track reconstruction for the ATLAS trigger HL-LHC upgrade. University of Geneva; 2021.

22. Jeżabek M, Kühn JH. QCD corrections to semileptonic decays of heavy quarks. Nucl Phys B. 1989;314(1):1–6.

23. Gao J, Li CS, Zhu HX. Top-quark decay at next-to-next-to-leading order in QCD. Phys Rev Lett. 2013;110(4):42001.

24. Group PD, Zyla Pa, Barnett RM, Beringer J, Dahl O, Dwyer DA, et al. Review of particle physics. Prog Theor Exp Phys. 2020;2020(8):083C01.

25. Czakon M, Fiedler P, Mitov A. Total top-quark pair-production cross section at hadron colliders through O (α S 4). Phys Rev Lett. 2013;110(25):252004.

26. Leyko A. Measurement of the top quark decay branching fraction ratio R b= B (t→ Wb)/B (t→ Wq) and of the inclusive production cross section pp→ tt in the dilepton channel at ATLAS. Universitäts-und Landesbibliothek Bonn; 2022.

27. Glashow SL, Iliopoulos J, Maiani L. Weak interactions with lepton-hadron symmetry. Phys Rev D. 1970;2(7):1285.

28. Aaltonen T, Adelman J, Akimoto T, Albrow MG, Gonzalez BA, Amerio S, et al. Search for the Flavor-Changing Neutral-Current Decay t→ Z q in p $\bar{p}$ Collisions at $\sqrt{s}$= 1.96 TeV. Phys Rev Lett. 2008;101(19):192002.

29. Abazov VM, Abbott B, Acharya BS, Adams M, Adams T, Alexeev GD, et al. Search for flavor changing neutral currents in decays of top quarks. Phys Lett B. 2011;701(3):313–20.

30. Onofre A. Searches for new physics in top decays at the LHC. arXiv Prepr arXiv12126898. 2012;

31. Tuovinen E, Hoffmann KH, Branca A, Vorobyev A, Pandolfi F, Rutherford B, et al. Search for Flavor-Changing Neutral Currents in Top-Quark Decays t→ Zq in pp Collisions at root s= 8 TeV. Phys Rev Lett. 2014;112(17).

32. Cakir O, Yilmaz A, Cakir IT, Senol A, Denizli H. Probing top quark FCNC tqγ and tqZ couplings at future electron-proton colliders. Nucl Phys B. 2019;944:114640.

33. Li CS, Oakes RJ, Yuan TC. QCD corrections to t→ W^+ b. Phys Rev D. 1991;43(11):3759.

34. Tanabashi M, Hagiwara K, Hikasa K, Nakamura K, Sumino Y, Takahashi F, et al. Review of particle physics. Phys Rev D. 2018;98(3):30001.

35. Brüning O, Seryi A, Verdú-Andrés S. Electron-Hadron Colliders: EIC, LHeC and FCC-eh. Front Phys. 2022;355.

36. Fernandez JLA, Adolphsen C, Akay AN, Aksakal H, Albacete JL, Alekhin S, et al. A large hadron electron collider at CERN report on the physics and design concepts for machine and detector. J Phys G Nucl Part Phys. 2012;39(7):75001.

37. Agostini P, Aksakal H, Alekhin S, Allport PP, Andari N, Andre KDJ, et al. The large hadron–electron collider at the HL-LHC. J Phys G Nucl Part Phys. 2021;48(11):110501.

38. Apollinari G, Béjar Alonso I, Brüning O, Fessia P, Lamont M, Rossi L, et al. High-Luminosity Large Hadron Collider (HL-LHC). Technical Design Report V. 0.1. Fermi National Accelerator Lab.(FNAL), Batavia, IL (United States); 2017.

39. Rossi L, Brüning O. Progress with the high luminosity LHC project at CERN. In: Proc 10th Int Partile Accel Conf. 2019. p. Australia.

40. Klein M. Future deep inelastic scattering with the LHeC. In: From My Vast Repertoire… Guido Altarelli's Legacy. World Scientific; 2019. p. 303–47.

41. Bruening O, Klein M. The large hadron electron collider. Mod Phys Lett A. 2013;28(16):1330011.

42. Bogacz SA, Holzer BJ, Osborne JA. An Energy Recovery Linac for the LHeC. arXiv preprint arXiv:2206.07678. 2022 Jun 15.

43. Agapov I, Benedikt M, Blondel A, Boscolo M, Brunner O, Llatas MC, Charles T, Denisov D, Fischer W, Gianfelice-Wendt E, Gutleber J. Future Circular Lepton Collider FCC-ee: Overview and Status. arXiv preprint arXiv:2203.08310. 2022 Mar 15.

44. Mangano M, Mccullough MP, Grojean C, Schwanenberger C, Selvaggi M, Helsens C, Ramsey-Musolf M, Blondel A, de Blas J, Dainese A, Poole J. FCC Physics Opportunities: Future Circular Collider Conceptual Design Report Volume 1. Eur. Phys. J. C. 2018 Dec 14;79(CERN-ACC-2018-0056):474.

45. FCC collaboration. FCC Physics Opportunities: Future Circular Collider Conceptual Design Report Volume 1. European Physical Journal C. 2019 Jun 1;79(6):474

46. Alwall J, Frederix R, Frixione S, Hirschi V, Maltoni F, Mattelaer O, Shao HS, Stelzer T, Torrielli P, Zaro M. The automated computation of tree-level and next-to-leading order differential cross sections, and their matching to parton shower simulations. Journal of High Energy Physics. 2014 Jul;2014(7):1-57.

47. Alloul A, Christensen ND, Degrande C, Duhr C, Fuks B. FeynRules 2.0—A complete toolbox for tree-level phenomenology. Computer Physics Communications.2014 Aug 1;185(8):2250-300.

48. Sjöstrand T, Mrenna S, Skands P. PYTHIA 6.4 physics and manual. Journal of High Energy Physics. 2006 May 9;2006(05):026.

49. Aaron FD, Abramowicz H, Abt I, Adamczyk L, Adamus M, Martin AD, Alexa C, Andreev V, Antonelli S, Antonioli P, Antonov A. Combined measurement and QCD analysis of the inclusive e±p scattering cross sections at HERA. Journal of High Energy Physics. 2010 Jan;2010(1):1-63.

50. Alwall J, Herquet M, Maltoni F, Mattelaer O, Stelzer T. MadGraph 5: going beyond. Journal of High Energy Physics. 2011 Jun;2011(6):1-40.

51. Sjöstrand T, Mrenna S, Skands P. A brief introduction to PYTHIA 8.1. Computer Physics Communications. 2008 Jun 1;178(11):852-67.

52. Murayama H, Watanabe I, Hagiwara K. HELAS: HELicity amplitude subroutines for Feynman diagram evaluations. National Lab. for High Energy Physics; 1992.

53. Maltoni F, Stelzer T. MadEvent: Automatic event generation with MadGraph. Journal of High Energy Physics. 2003 Feb 21;2003(02):027.

54. Degrande C, Duhr C, Fuks B, Grellscheid D, Mattelaer O, Reiter T. UFO–the universal FeynRules output. Computer Physics Communications. 2012 Jun 1;183(6):1201-14.56. Tanabashi M. Particle data group. Phys. Rev. D. 2018;98(3):030001.

55. Tanabashi M, Hagiwara K, Hikasa K, Nakamura K, Sumino Y, Takahashi F, Tanaka J, Agashe K, Aielli G, Amsler C, Antonelli M. Review of particle physics. Physical Review D. 2018 Aug 17;98(3):030001.

56. Sirunyan AM, Tumasyan A, Adam W, Asilar E, Bergauer T, Brandstetter J, Brondolin E, Dragicevic M, Erö J, Flechl M, Friedl M. Search for associated production of a Z boson with a single top quark and for tZ flavour-changing interactions in pp collisions at s= 8√ s= 8 TeV. Journal of High Energy Physics. 2017 Jul;2017(7):1-43.

57. Rosten R. New Physics at HL-LHC with ATLAS. ATL-COM-PHYS-2017-1749; 2018 Feb 1.

58. Aguilar–Saavedra JA. Ultraboosted Zt and γ_t γ t production at the HL-LHC and FCC-hh.

The European Physical Journal C. 2017 Nov;77(11):1-7.

-